

# REPORT DOCUMENTATION PAGE

AFRL-SR-AR-TR-03-

Public reporting burden for this collection of information is estimated to average 1 hour per response, including the time for reviewing instructions, searching existing data sources, gathering the required data, completing and reviewing this collection of information. Send comments regarding this burden estimate or any other aspect of this collection of information, including suggestions for reducing this burden, to Washington Headquarters Services, Directorate for Information Operations and Reports (0704-0188). Respondents should be aware that notwithstanding any other provision of law, no person shall be subject to any penalty for failing to comply with a collection of information if it does not have a valid OMB control number. PLEASE DO NOT RETURN YOUR FORM TO THE ABOVE ADDRESS.

0155

re  
ig  
ntly

<b>1. REPORT DATE (DD-MM-YYYY)</b> 30-12-2002		<b>2. REPORT TYPE</b> Final Report		<b>3. DATES COVERED (From - To)</b> 01-10-1999 - 30-09-2002	
<b>4. TITLE AND SUBTITLE</b> IMPROVING THE PERFORMANCE OF AIR FORCE ADAPTIVE OPTICS SYSTEMS USING HIGH-RESOLUTION SPATIAL LIGHT MODULATORS WITH DEFORMABLE MIRRORS: FINAL REPORT				<b>5a. CONTRACT NUMBER</b> F49620-99-1-0342	
				<b>5b. GRANT NUMBER</b>	
				<b>5c. PROGRAM ELEMENT NUMBER</b>	
<b>6. AUTHOR(S)</b> Michael K. Giles, Mikhail Vorontsov, and Michael Roggemann				<b>5d. PROJECT NUMBER</b>	
				<b>5e. TASK NUMBER</b>	
				<b>5f. WORK UNIT NUMBER</b>	
<b>7. PERFORMING ORGANIZATION NAME(S) AND ADDRESS(ES)</b> New Mexico State University Box 30001, MSC 3-0 Las Cruces, NM 88003				<b>8. PERFORMING ORGANIZATION REPORT NUMBER</b>	
<b>9. SPONSORING / MONITORING AGENCY NAME(S) AND ADDRESS(ES)</b> Air Force Office of Scientific Research 801 North Randolph Room 732 Arlington, VA 22203-1977				<b>10. SPONSOR/MONITOR'S ACRONYM(S)</b> AFOSR	
				<b>11. SPONSOR/MONITOR'S REPORT NUMBER(S)</b>	
<b>12. DISTRIBUTION / AVAILABILITY STATEMENT</b> Dr. Jon Sjogren AFOSR/NM Arlington, VA 22203-1977 Tel: 703-696-6564  Approved for public release, distribution unlimited					
<b>13. SUPPLEMENTARY NOTES</b>					
<b>14. ABSTRACT</b> This document presents a comprehensive technical summary of the most significant work accomplished on Air Force Office of Scientific Research Contract Number F49620-99-1-0342. Since closed loop wave front control (WFC) systems currently being developed by the Air Force have residual wave front errors that reduce image quality, New Mexico State University has developed methods to reduce those residual errors and improve the quality (Strehl ratio) of Air Force WFC systems. Our approach is to develop concepts that utilize high-resolution spatial light modulators to improve the achievable system Strehl ratio. Two such concepts are (a) high resolution secondary WFC loops, and (b) reconfigurable Shack-Hartmann wave front sensors (RSHS) based on liquid crystal devices (LCD). A high-resolution adaptive optics test bed has been developed at NMSU using LCD's extracted from LCD projectors, and it has been used successfully to test both the secondary loop and RSHS concepts. Results indicate that both concepts improve system performance.					
<b>15. SUBJECT TERMS</b> wave front sensing, wave front control, adaptive optics					
<b>16. SECURITY CLASSIFICATION OF:</b>			<b>17. LIMITATION OF ABSTRACT</b>	<b>18. NUMBER OF PAGES</b>  42	<b>19a. NAME OF RESPONSIBLE PERSON</b> Michael K. Giles
<b>a. REPORT</b> unclassified	<b>b. ABSTRACT</b> unclassified	<b>c. THIS PAGE</b> unclassified			<b>19b. TELEPHONE NUMBER (include area code)</b> 505-646-3833

Standard Form 298 (Rev. 8-98)  
Prescribed by ANSI Std. Z39.18

20030513 078

# **IMPROVING THE PERFORMANCE OF AIR FORCE ADAPTIVE OPTICS SYSTEMS USING HIGH-RESOLUTION SPATIAL LIGHT MODULATORS WITH DEFORMABLE MIRRORS: FINAL REPORT**

## **1. Executive Summary**

This document presents a comprehensive technical summary of the most significant work accomplished on Air Force Office of Scientific Research Contract Number F49620-99-1-0342, "Improving the performance of Air Force adaptive optics systems using high-resolution spatial light modulators with deformable mirrors." Since closed loop wave front control (WFC) systems currently being developed by the Air Force have residual wave front errors that reduce image quality, New Mexico State University has developed methods to reduce those residual errors and improve the quality (Strehl ratio) of Air Force WFC systems. Our approach is to develop concepts that utilize high-resolution spatial light modulators to improve the achievable system Strehl ratio. Two such concepts are (a) high resolution secondary WFC loops, and (b) reconfigurable Shack-Hartmann wave front sensors (RSHS) based on liquid crystal devices (LCD). A high-resolution adaptive optics test bed has been developed at NMSU using LCD's extracted from LCD projectors, and it has been used successfully to test both the secondary loop and RSHS concepts. Results indicate that both concepts improve system performance. This work was done by Dr. Michael K. Giles, co-director of NMSU's Electro-Optics Research Laboratory, in cooperation with Dr. Mikhail Vorontsov, director of the Army Research Laboratory's Intelligent Optics Laboratory in Adelphi, Maryland, and Co-PI of this project, a service he provided free of charge. Dr. Michael Roggemann of Michigan Technological University (MTU) was included as a subcontractor on this project during FY2001 and FY2002.

The most significant technical accomplishments of this work are the following:

- (1) Experimental performance analysis of a high-resolution wave front control system with a MEMS deformable mirror.
- (2) Experimental performance analysis of a high-resolution secondary wave front control loop with a LCD wave front corrector working in concert with a phase-contrast LCD-based Zernike filter wave front sensor. Simulated primary loop data with residual wave front errors was used as input to the secondary loop, thus demonstrating the utility of a secondary loop.
- (3) Experimental performance analysis of a reconfigurable Shack-Hartmann wave front sensor (RSHS) using a dynamic lenslet array written on a projector LCD,
- (4) A new approach to controlling a deformable mirror in beam projection systems operating in conditions of strong turbulence was introduced. It has been shown that the nonlinear optimization of an image sharpness metric can significantly improve the performance of the beam projection system.

Item (1) was completed at the U. S. Army Research Laboratory's Intelligent Optics Laboratory, items (2) and (3) were completed at NMSU's Electro-Optics Research Laboratory, and item (4) was completed at Michigan Technological University. The simulated primary loop data for Item (2) were also provided by MTU. Complete descriptions of the experimental equipment, set up, and procedures for each of the four items listed above are contained in sections 2, 3, 4, and 5, respectively.

The specific references for each topic are included in the order cited at the end of the respective sections, but a complete bibliography is also included as the last section in the report. Ten papers have been published as a direct result of this work. They are listed in bold as numbers 1 through 10 in the complete bibliography on pages 41 and 42 of this report. We should mention that at least three additional papers based on this contract, but not listed in the bibliography, are being prepared for publication within the coming year.

This work has supported two Postdoctoral Fellow (Dr. Thomas Weyrauch and Dr. Sarah John at the Army Research Laboratory), three Ph.D. students (Tony Seward, Chueh Ting, and Jungtae Rha at NMSU) and three Masters students (Ray Jimenez at NMSU and two students at MTU). Mr. Rha just defended his Ph.D. dissertation titled "Wave Front Sensing and Reconstruction Using a Twisted Nematic Liquid Crystal Device" on December 11, 2002.

## 2. Experimental performance analysis of a high-resolution wavefront control system with a MEMS deformable mirror

We investigated the performance of an adaptive optical system consisting of two separate control loops for large-scale (tip and tilt) and higher order wavefront distortions. Tip and tilt correction was performed using a piezoelectric actuated mirror and a linear position sensitive detector (PSD). The secondary control loop uses a MEMS deformable mirror as high-resolution wavefront corrector and the stochastic parallel gradient descent (SPGD) algorithm for model-free optimization of a system performance metric (e.g. Strehl ratio).

The investigations comprised the following steps:

- Evaluation of MEMS mirrors
- Adapting of a SPGD controller for controlling MEMS mirrors
- Optimizing controller hard- and software
- Set-up of the adaptive optics system with two control loops
- Tests with laboratory generated turbulence
- Performance evaluation with laser beams propagating through atmospheric turbulence

### 2.1. High Resolution Wavefront Control System

#### 2.1.1. MEMS Mirrors

Deformable mirrors (DMs) based on MEMS technology are expected to replace conventional DMs due to low-cost manufacturing. The use of MEMS deformable mirrors ( $\mu$ DMs) will however only be possible if their optical and mechanical properties match those of conventional DMs. We compared thus several different  $\mu$ DM technology approaches esp. with respect to the used SPGD control strategy [1-3].

Table 2.1 summarizes basic design parameters and important experimental results for all mirrors under investigation. Three basically different design strategies were used for the  $\mu$ DMs:

- The OKO mirror (from Flexible Optical B.V., The Netherlands) consists of a micromachined  $\mu$ m-thick membrane attached to a PCB with the electrode structure (Fig. 2.1 f). The active area has a diameter of 12 mm.
- The  $\mu$ DMs from MEMSOptical ( $MO_z$ ,  $MO_s$ ) and the University of Colorado (UC) have small mirror areas attached to the substrate by flexures of different shape (Fig. 2.1. b, c, e, respectively). Flexures and mirror consist of aluminum ( $MO$  mirrors) or polysilicon with additional reflective layer (UC). The center-to-center distance between actuators is 500  $\mu$ m and 250  $\mu$ m for the  $MO$  and UC mirrors, respectively. Because of the low fill factor lenslet arrays have to be used with these  $\mu$ DMs. The main advantage of their design is the low operation voltage.
- The  $\mu$ DMs from Boston University have the actual mirror membrane attached to the actuators by attachment posts. The membrane can be continuous ( $BU_{12TT}$ ), segmented with each segment attached to one actuator allowing a piston type movement ( $BU_{12P}$ ), and a segmented membrane with four corners of adjacent segments attached to one actuator allowing for tip-tilt as well as piston movement ( $BU_{tt}$  and  $BU_{12TT}$ , Fig. 2.1 a, d).  $BU_{tt}$  was a prototype with 250  $\mu$ m segment size and 5x5 actuators, the  $BU_{12}$  mirrors have 140 actuators (12x12 without the corner elements) with 300  $\mu$ m segments. These mirrors require high voltage (200 – 300 V).



**Table 2.1:** Summary of mirror properties [1,3]

	<b>T</b>	<b>N</b>	$d_M$	$d_P$	$U$	$d_S$ ( $\mu\text{m}$ )	$v_{\text{res}}$ (kHz)	$v_{3\text{dB}}$ (kHz)
<b>OKO</b>	CM	37	12 mm active aperture	1.75 mm (hexagonal)	0-210 V	6	2	-
<b>MO<sub>z</sub></b>	P	36	160 $\mu\text{m}$	500 $\mu\text{m}$ (rectangular)	0-15 V	0.7	5.8	-
<b>MO<sub>s</sub></b>	P	36	100 $\mu\text{m}$	500 $\mu\text{m}$ (rectangular)	0-30 V	1.1	5.3	-
<b>UC</b>	P	128	74 $\mu\text{m}$	250 $\mu\text{m}$ (rectangular)	0-11 V	0.9	-	6
<b>BU<sub>tt</sub></b>	TT	25	242 $\mu\text{m}$	250 $\mu\text{m}$ (rectangular)	0-300 V	0.9	-	24
<b>BU<sub>12M</sub></b>	CM	140	300 $\mu\text{m}$	300 $\mu\text{m}$ (rectangular)	0-200 V	2	-	7.5
<b>BU<sub>12TT</sub></b>	TT	140	292 $\mu\text{m}$	300 $\mu\text{m}$ (rectangular)	0-200 V	2	-	12
<b>BU<sub>12P</sub></b>	P	140	292 $\mu\text{m}$	300 $\mu\text{m}$ (rectangular)	0-200 V	2	-	18

(T type of motion (P piston, TT tip-tilt, M continuous membrane), N number of actuators,  $d_M$  size of mirror,  $d_P$  actuator pitch,  $U$  actuator voltage range  $d_S$  actuator stroke,  $v_{\text{res}}$  resonance frequency,  $v_{3\text{dB}}$  3dB bandwidth)

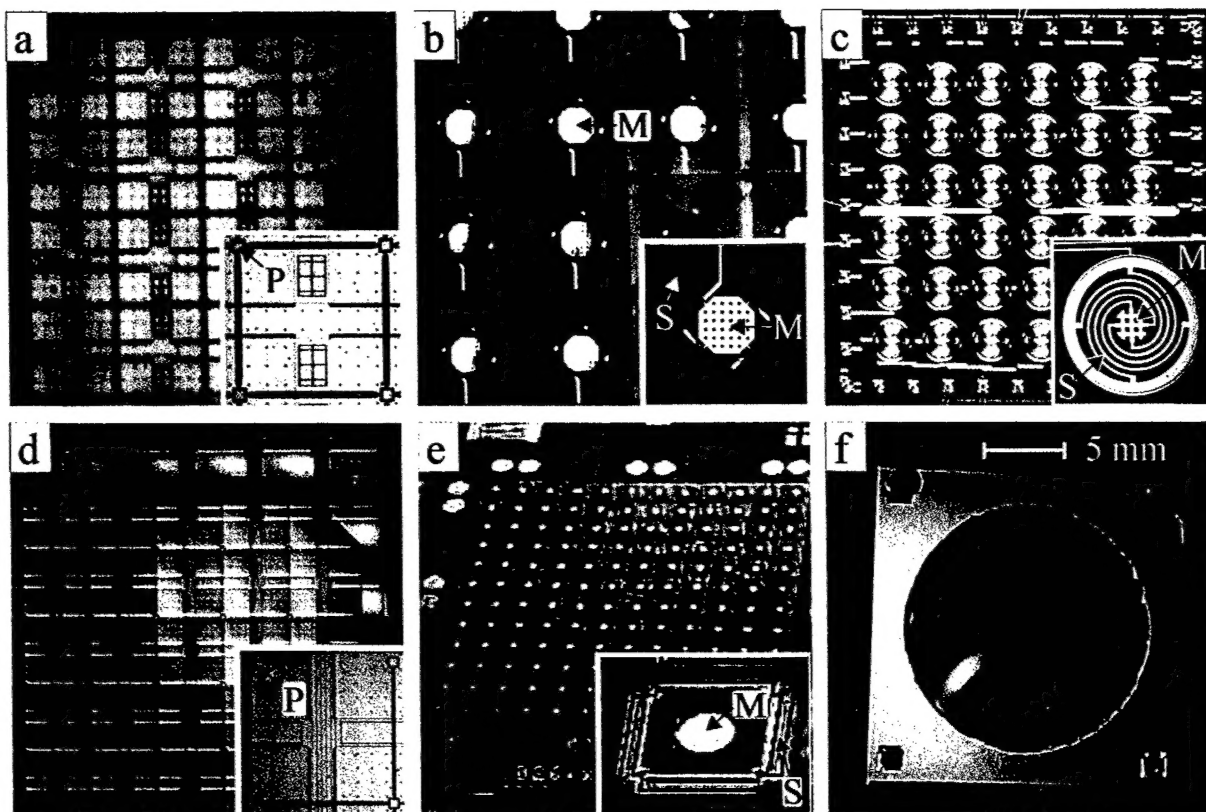


**Fig. 2.1.** Microscope images of different MEMS deformable mirrors. a)  $BU_{tt}$ , b)  $Mo_z$ , c)  $Mo_s$ , d)  $BU_{12TT}$ , e) UC, f) OKO (M=mirror, S=spring, P=attachment post) [3].

Interferometer images and far field pattern of three different mirrors ( $BU_{tt}$ ,  $BU_{12TT}$ ,  $MO_s$ ) are shown in Fig. 2.2. They demonstrate that the optical quality is not yet satisfactory. The BU mirrors show print-through pattern from the underlying actuator structure whereas in case of the  $MO_s$  mirror the lenslet array is a limiting factor.

The dynamic range of the different mirrors is demonstrated in Fig. 2.3. The OKO,  $MO_z$  and  $MO_s$  mirrors show pronounced resonance behavior, they can be used for frequencies up to 1 kHz (OKO) or 3 kHz (MO). The UC mirrors has a strongly damped frequency response curve. Fastest response is provided by the  $BU_{tt}$   $\mu$ DM (the 3dB bandwidth is about 24 kHz), but its design allows only small stroke. The slightly different  $BU_{12TT}$  mirror with larger stroke has a bandwidth of about 18 kHz. The piston type  $BU_{12P}$  shows a very weak resonance and the  $BU_{12CM}$   $\mu$ DM with a continuous membrane the lowest bandwidth of the BU mirror family.

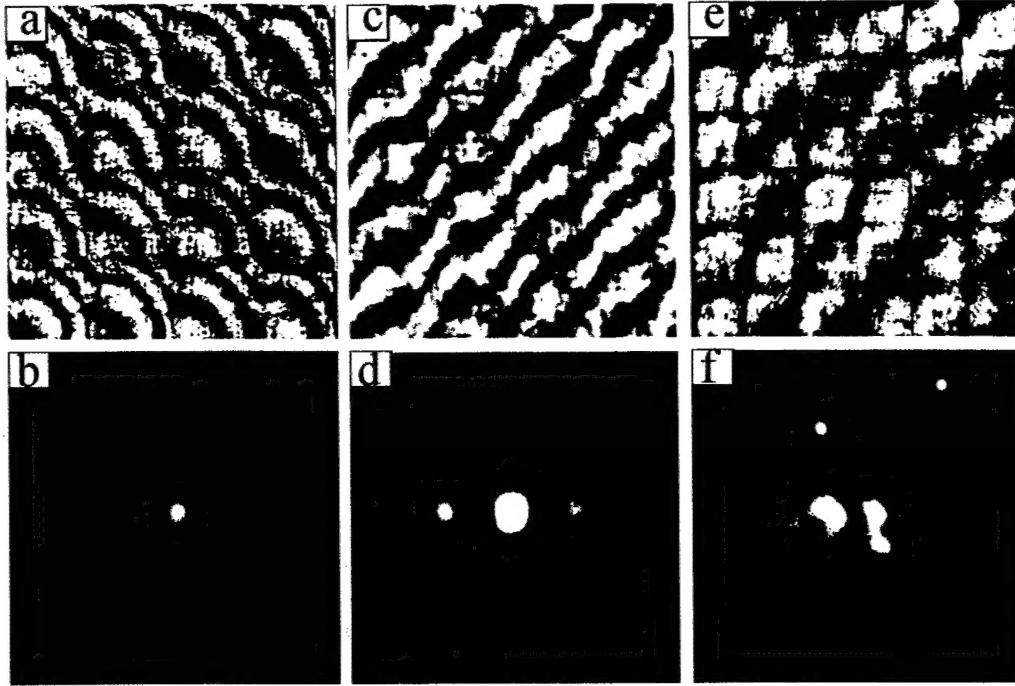


**Fig. 2.2.** Interferometer images of mirror surface (a, c, e) and far-field pattern (b, d, f) of mirrors BU<sub>tt</sub> (a, b), BU<sub>12TT</sub> (c, d), MO<sub>s</sub> with lenslet array (e, f) with no voltage applied [3].

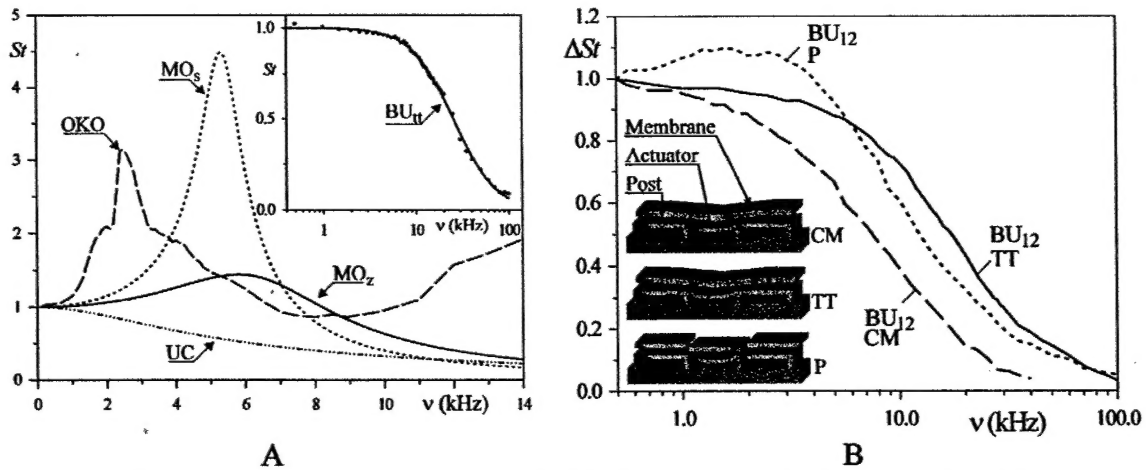


**Fig. 2.3.** Frequency response curves of MEMS mirrors under investigation [3].

### 2.1.2. SPGD Controller

The SPGD wavefront controller used for the investigations consists of supervisory controller and seven VLSI chips (*AdOpt* system) that implement the stochastic parallel gradient-descent algorithm for optimization of a scalar performance metric (Strehl ratio). The controller chips generate at each iteration step  $n$  statistically independent control parameter perturbations  $\{\delta u_j^{(n)}\}$  in parallel for all  $N$  control voltages  $\{u_j^{(n)}\}$ , where

$j = 1, \dots, N$ . The perturbations have the same absolute value  $\sigma$  but pseudo-random sign, thus  $\langle \delta u_j \delta u_k \rangle = \sigma^2 \delta_{jk}$ , where  $\delta_{jk} = (1, \text{ for } j=k; 0, \text{ otherwise})$  is the Kronecker symbol. After application of the control voltage perturbations to the MEMS mirror the system measures a perturbed metric value (here usually the Strehl ratio)  $P_+^{(n)}$ . Then the signs of all perturbation voltages are inverted and the corresponding metric value  $P_-^{(n)}$  is measured, i.e.

$$P_{\pm}^{(n)} = P(u_1^{(n)} \pm \delta u_1^{(n)}, \dots, u_j^{(n)} \pm \delta u_j^{(n)}, \dots, u_N^{(n)} \pm \delta u_N^{(n)}) . \quad (1)$$

The control voltages are then updated according to the rule

$$u_j^{(n+1)} = u_j^{(n)} + \gamma [P_+^{(n)} - P_-^{(n)}] \text{sign}[\delta u_j^{(n)}] \quad (2)$$

with an appropriately chosen update coefficient  $\gamma$ . The system performs maximization or minimization of the metric  $P$  depending on the sign of  $\gamma$ .

A PC equipped with digital/analog in- and outputs was used for supervisory control although the *AdOpt* system is designed to use a PIC controller for this purpose. The PC allowed for an easier software development and was also used for data acquisition to evaluate the system performance. With a fast PC (1 GHz) and optimization of the *AdOpt* control algorithm an iteration rate of 11.5 kHz was achieved, where the limiting factors were the response of the MEMS mirror (BU<sub>tt</sub>) and the high voltage amplifier [2-4].

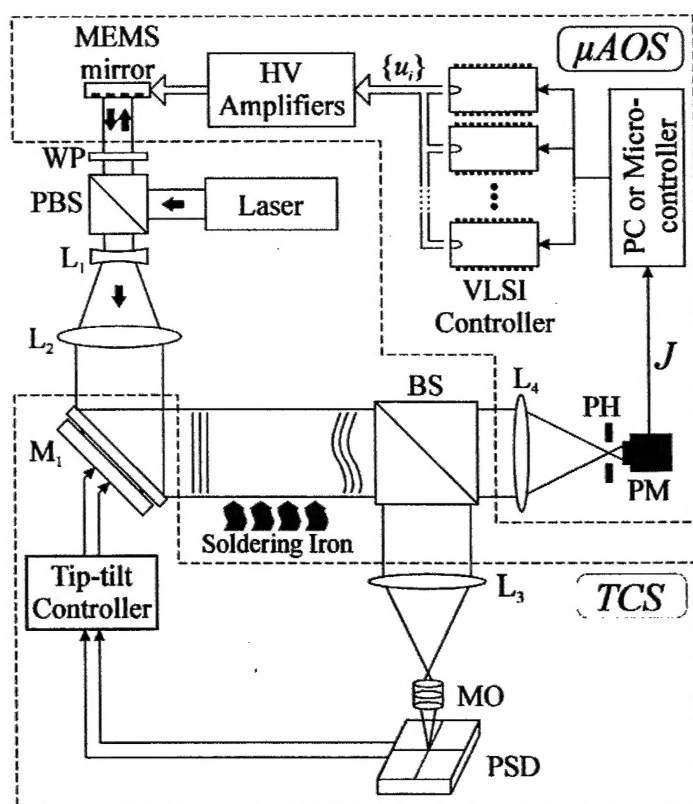
### 2.1.3. Adaptive Optics System Laboratory Test

Fig. 2.4 shows a schematic of the AO system used for laboratory tests [4]. It was composed of two subsystems: a 132-channel micro-scale (MEMS mirror/VLSI controller) adaptive system ( $\mu$ AOS) and a 2-axis wave-front tilt control system (TCS). A linearly polarized input beam (3 mm diameter) from a laser-diode ( $\lambda=690$  nm) was reflected from polarizing beam splitter PBS and directed to the MEMS mirror. After reflection from MEMS mirror and double pass through  $\lambda/4$ -waveplate WP the input wave polarization was changed to orthogonal and passed through beam splitter without energy loss. To introduce small-scale dynamic phase distortions the beam size was expanded to 12 mm diameter by the lens system  $L_1$  and  $L_2$ . The expanded beam was reflected from the tip-tilt mirror  $M_1$  and passed through a turbulent region. We used two soldering irons and a metal grid with a cell size of 1 mm placed 40 mm below the laser beam for generation of a turbulent airflow. A small fan was used to increase the air convection speed in the area of the laser beam. The distorted beam was divided by about 50% using the beam splitter BS<sub>1</sub> and sent (after passing the lenses  $L_3$  and  $L_4$ ) to both TCS and  $\mu$ AOS system photo-detectors.

Wave-front tilts were compensated using a beam control system based on a beam steering mirror (Physik Instrumente) and position sensitive detector (PSD) from Pacific Silicon Sensor, Inc. The focal plane of lens  $L_1$  was imaged by the microscope objective MO onto the surface of the PSD (a duo-lateral photodiode with a  $10 \times 10$  mm<sup>2</sup> active area) thus providing measurements of the focused beam  $x$ - and  $y$ -centroid coordinates. The

corresponding  $x$ - and  $y$ -position signals from the PSD were used as feedback signals to compensate wave-front tilts and stabilize the laser beam focal spot position in the center of the PSD. The tilt control system closed-loop bandwidth was near 300 Hz.

The  $\mu AOS$  included a  $BU_{12TT}$  MEMS mirror and the *AdOpt* VLSI controller. The 132 control channels were connected to the same number out of 140 mirror elements in such a way that a circular controllable aperture was provided. As the system performance metric  $J$  we used the light power inside the 50- $\mu m$  pinhole PH placed in the lens focal plane and measured by a photo-multiplier. This metric  $J$  is proportional to the Strehl ratio  $St$  commonly used in adaptive optics. The values of the performance metric  $J$  were used for on-chip computations of the control voltages  $\{u_i\}$  ( $i=1, \dots, 132$ ). These control voltages were amplified by a set of high-voltage amplifiers (in the range of 0 to 200 V) and applied to the MEMS mirror electrodes.



**Fig. 2.4.** Adaptive optics systems used for laboratory experiments with the tilt control system *TCS* and the high-resolution micro-scale adaptive optics system  $\mu AOS$  [4].

The parallel analog on-chip control voltage computations and the high (near 17 kHz) micro-mirror array bandwidth allowed for the first time a sub-millisecond wavefront correction rate - the system performed 11,000 control voltages updates (iterations) per second. This fast iteration rate enabled the demonstration of real-time adaptive correction of turbulence induced wave-front phase distortions. Fig. 2.5 summarizes the main results of the experiments. It shows the probability density functions of the performance metric  $J$  for different wavefront distortion compensation conditions:



- Curve 1: Both, *TCS* and  $\mu AOS$ , were off; turbulence generation was on  
 Curve 2: Only  $\mu AOS$  was on (*TCS* was off); turbulence generation was on  
 Curve 3: Only *TCS* was on ( $\mu AOS$  was off); turbulence generation was on  
 Curve 4: Both, *TCS* and  $\mu AOS$ , were on; turbulence generation was on  
 Curve 5: Both, *TCS* and  $\mu AOS$ , were on; turbulence generation was off

In the absence of adaptation the probability density function (curve 1) is wide indicating a high level of the intensity scintillations. The compensation of wave-front tilts only (curve 3) resulted in an increase of the averaged intensity level  $\langle J \rangle$  (shift of the PDF curve maximum). This compensation of just wave-front tilts had almost no impact on the intensity scintillation level; the probability density functions without adaptation and with tilt-only compensation have approximately the same width. This can be explained by the presence of strong higher order aberrations resulting in the appearance of several spots in the focal intensity distribution. The tilt control system is not able to change the intensity distribution itself and instead moves the entire beam so as to place the most closely located intensity spot inside pinhole. Adaptive compensation of high order aberrations using the  $\mu AOS$  (curve 2) resulted in a noticeable decrease of the intensity scintillation level (narrowing the probability density function) if compared with the PDF curves corresponding to the absence of adaptation or to the tilt control PDF curve in Fig. 2.5. The high order aberration compensation with the  $\mu AOS$  provided formation of a single focal plane spot thus decreasing the intensity scintillation level. The compensation of both wave-front tilts and high order aberrations resulted in a further (approximately two-fold) increase of the average metric value.

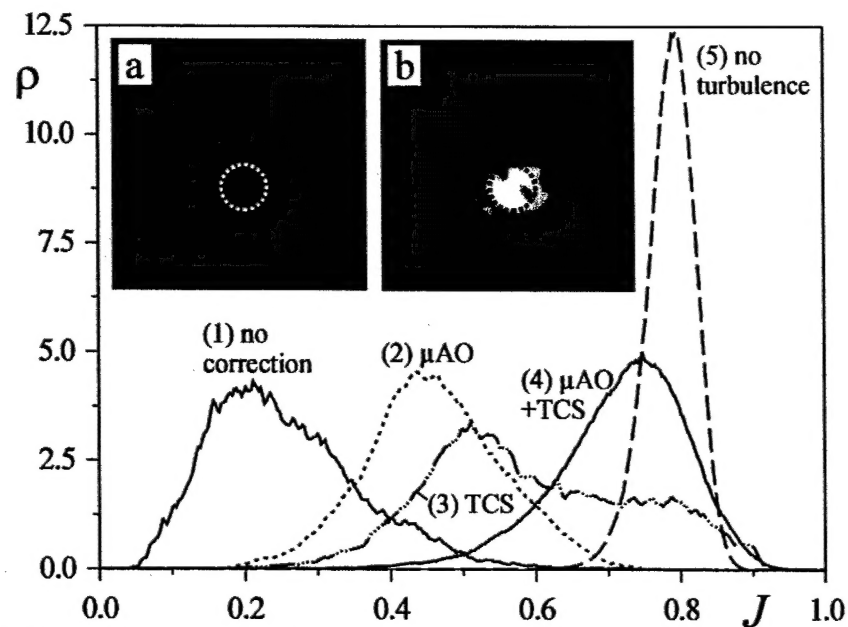


**Fig. 2.5.** Probability density functions  $\rho$  of the performance metric  $J$  for different operation conditions of the adaptive optics system. The images a and b show an averaged intensity distribution in the focal plane of lens  $L_4$  (location of pinhole PH) with the adaptive system off and on, respectively. The dotted circle demonstrates the size of the pinhole [4].

For comparison we also measured the probability distribution functions in the system without turbulence (curve 5), which corresponds to the optimal adaptation level that can be achieved. This "turbulence-free" PDF curve is still quite wide (about half as wide as the corresponding curve with turbulence present). The intensity (metric) scintillations causing the PDF curve widening in the absence of turbulence result from wave-front phase perturbations introduced by the  $\mu AOS$  system itself. Indeed, in the absence of both turbulence and adaptation (no applied perturbations), the probability distribution curve (not shown in Fig. 2.5) is almost 3 times narrower than curve 5.

The frame-averaged focal plane intensity distributions without correction and with adaptive compensation (both *TCS* and  $\mu AOS$  system are on) are also shown in Fig. 2.5 as inset images, a and b, respectively. For frame averaging we used 50 intensity distributions taken in intervals of 1 second. The pinhole position is shown by the dotted circle corresponding to the pinhole diameter of 50  $\mu m$ . Analysis of the experimental data shows that simultaneous correction of both wave-front tilts and higher order aberrations allowed near 92% of the maximum possible average metric value  $\langle J \rangle$  corresponding to undistorted conditions to be achieved. The normalized standard deviation of the beam quality metric  $\sigma_J$  was decreased from 0.41 for the uncorrected case to 0.13 using the *TCS* and  $\mu AO$  systems simultaneously.

## 2.2. System Performance Evaluation with Atmospheric Propagation

For tests on ARL's atmospheric laser optics testbed (A-LOT) the system was modified [5], see Fig. 2.6. The light source (laser diode LD) with a collimating lens was placed on a water tower in 2.3 km distance from the laboratory building. To avoid beam steering a diffuser was placed in front of the laser diode. A telescope built from lenses L1, L2 and a periscope-like structure comprising mirrors M1, M2 collected the light and redirected it onto an optical table in the laboratory.

The primary control loop included now an additional beam steering mirror (slow, but with large angle) to allow for compensation of wavefront tilts induced by a relative misalignment of mirrors M1 (inside a shed on the roof of the building) and M2 (on the optical table) due to thermal expansion, etc. M2 was adjusted by the tip-tilt controller in such a way that the average angles of the fast piezoelectric actuated mirror M3 were kept in the middle of their dynamic range. The secondary control loop used the power  $P$  of the light that could be coupled into a single-mode fiber placed in the focal plane F10 of lens L10 as feedback signal for the *AdOpt* VLSI controller. This metric  $P$  can be considered as a good approximation for the Strehl ratio.

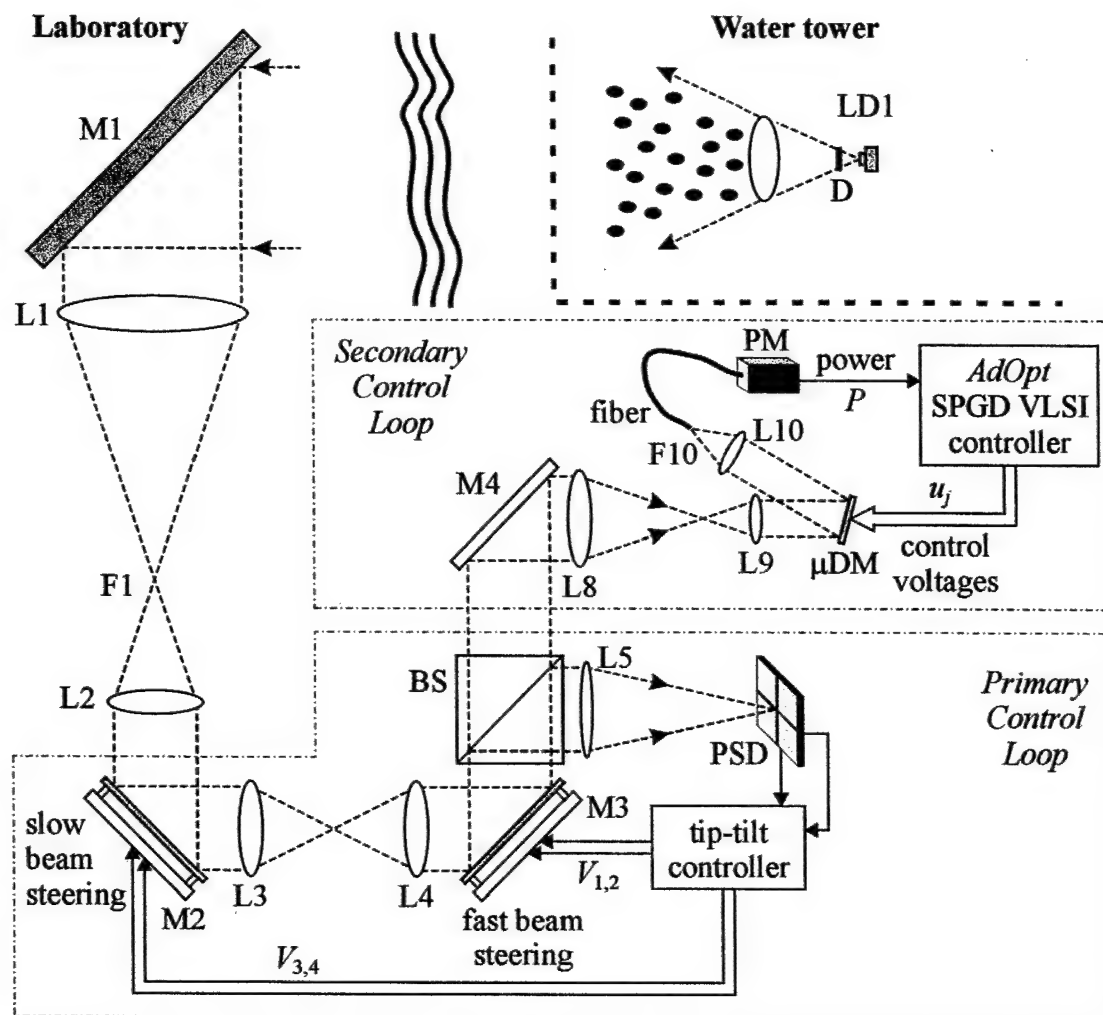


**Fig. 2.6.** Schematic of the AO system used with ARL's atmospheric laser optics testbed [5]

### 2.2.1. Primary Control Loop Test: Wavefront Tip-Tilt Correction

Figure 2.7 a shows the trace of the tip and tilt angle measured during a 2 second interval without beam steering. From a time series of tip-tilt angle measurements during a 3-minute period we calculated the corresponding probability density function (PDF), which is presented in Fig. 2.8 (denoted "off"). Wave front distortions from atmospheric turbulence as well as vibrations are the main contributions to the tip-tilt variations during this short-term measurement. Longer observation times reveal a slower motion due to thermal expansion etc. that have a much larger scale (exceeding  $250 \mu\text{rad}$ ). After turning on beam steering, the variation of tip and tilt is strongly reduced (Fig. 2.7 b), the corresponding PDF (Fig. 2.8 "on") is much narrower. The residual beam deviation angle was calculated from the PDF to about  $3 \mu\text{rad}$  [5].

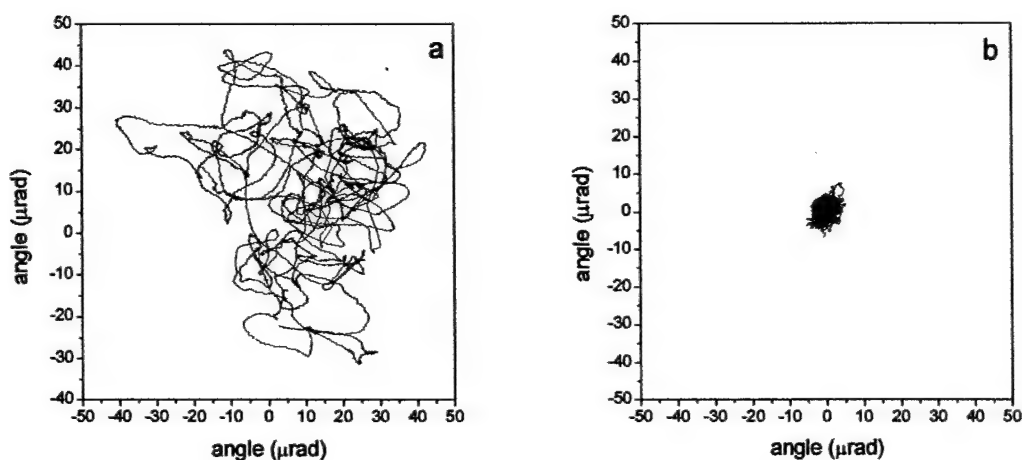


**Fig. 2.7.** Trace of the measured tip and tilt angles in the entrance pupil during a 2 second interval with the beam steering system off (a) and on (b).

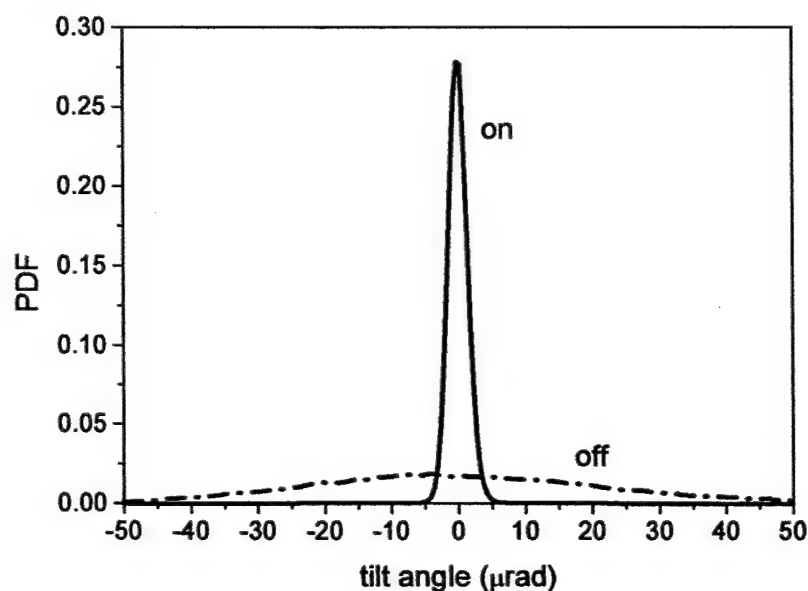


**Fig. 2.8.** Probability density function (PDF) for the measured tilt angle with beam steering on and off (acquired during a 3-minute interval)

### 2.2.2. High Resolution Wavefront Correction

Due to the long horizontal propagation in atmospheric turbulence a highly scintillated signal was received in the entrance pupil (lens L1); Fig. 2.9 a depicts the intensity distribution in this plane. The atmospheric distortions those introduced by the diffuser prevent an efficient focusing of the beam. The intensity distribution in the focal plane of lens L10 (a snapshot is shown in Fig. 2.9 b) is thus much wider than the distribution of an undistorted reference beam (the light from a single-mode fiber placed

in the focal plane F1 of lens L1), which is shown for comparison in Fig. 2.9 c with the same scale. The refractive index structure constant  $C_n^2$  was about  $2 \times 10^{-14} \text{ m}^{-2/3}$  when images 2.9 a and 2.9 b were taken.

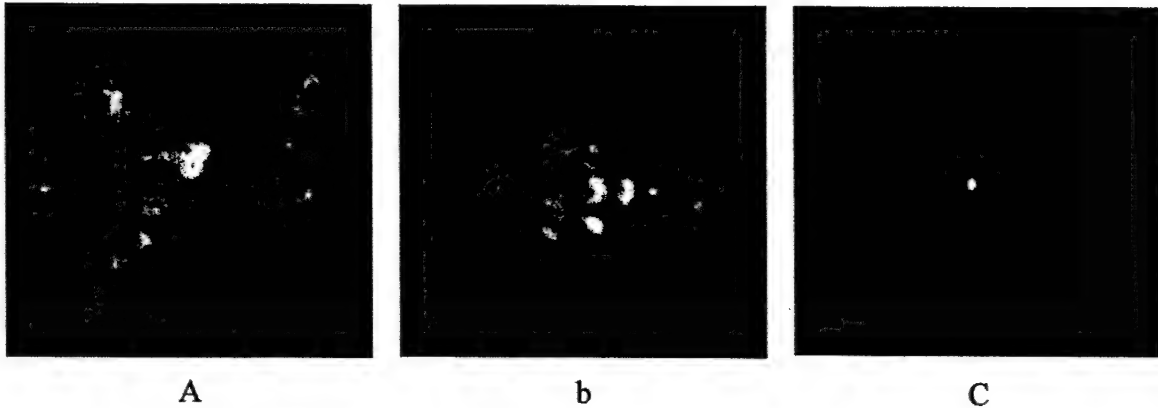


**Fig. 2.9.** Intensity distributions in the pupil plane of lens L1 (a) and the focal plane F10 of lens L10 (b). The focal spot obtained with a reference beam from a single-mode fiber located in the focal plane F1 of lens L1 is shown in (c) for comparison [5].

The amount of light that could actually be coupled into the fiber was subject to strong fluctuations because of the rapid change of the optical field in pupil and focal plane. Figure 2.10 a shows a sample time series of power measurements, taken when the SPGD AO system was off and tip-tilt control on. The power spectrum, which is shown in Fig. 2.10 b was obtained by averaging the spectra of 1000 subsequent measurements. The power values are normalized to the d.c. component. The spectrum reveals frequency components up to about 500 Hz.



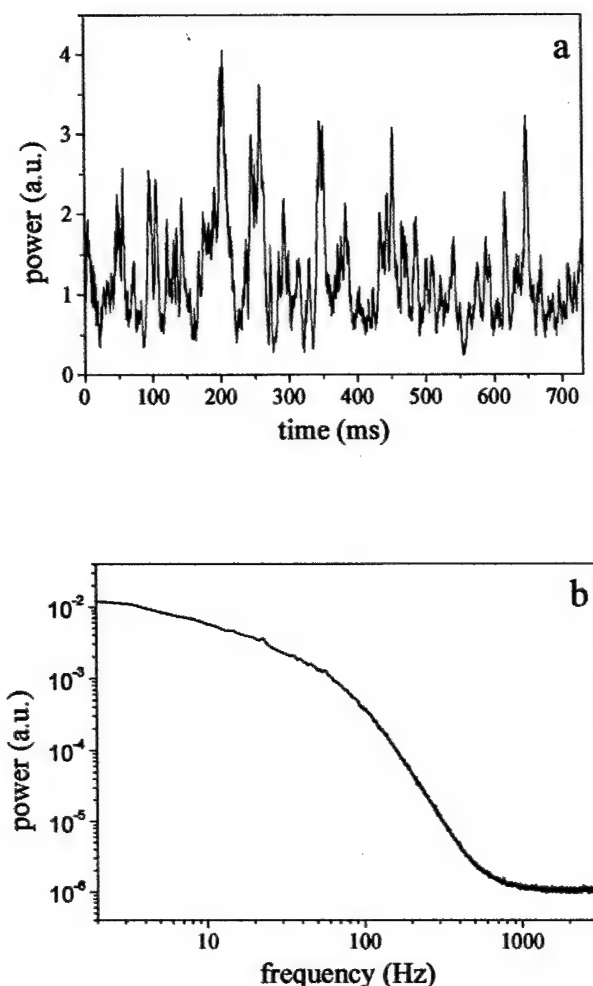


**Fig. 2.10.** a) Sample time series of metric measurements (optical power coupled into the fiber). b) Averaged power spectrum [5].

The (long-term) power fluctuation of the laser light that irradiated the entrance pupil made it difficult to compare the received power level with and without adaptive optics in the experiment with real atmospheric propagation. To suppress long-term effects the power was measured in short intervals (about 700 ms), where the high-resolution AO system (i.e. the MEMS/VLSI system) was off in the first half and on in the second half [5], see Fig. 2.11. This was repeated for 1000 times with a short break between the measurements for saving. The tip-tilt control system was on during the whole measurement time. Then the average power for the intervals as well as the probability density function (PDF) for power values with and without the SPGD AO system working were calculated.

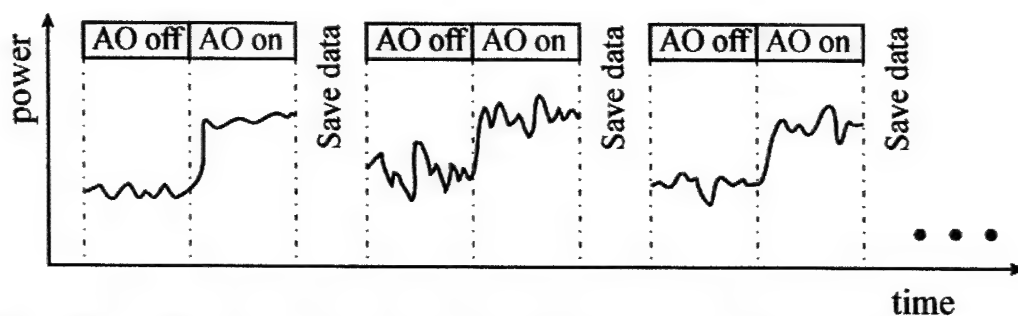


**Fig. 2.11.** Procedure for testing the performance of distortion compensation: Power values are recorded during short (about 0.7 s) intervals. The SPGD AO system is off during the first half of the period and on during the second half. A break between the intervals is used for saving data.

The results for two different experimental conditions (coupling into a single-mode and into a multi-mode fiber) are shown in Fig. 2.12. For the case of the single-mode fiber the secondary high-resolution AO system improved the average fiber coupling efficiency by about 50 % (Fig. 2.12 a). As can be seen from the probability density functions for the power levels (Fig. 2.12 b) high-power values become much more likely with the secondary loop working.

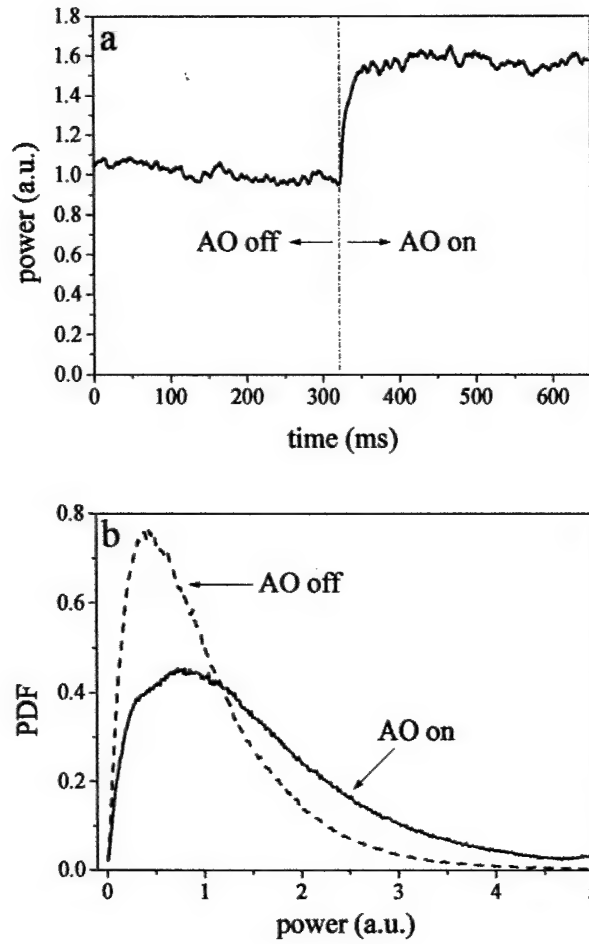


**Fig. 2.12.** Averaged evolution curve of the power coupled into the fiber (a) and experimental probability density functions for power values with the high-resolution secondary control loop on and off (b) [5].

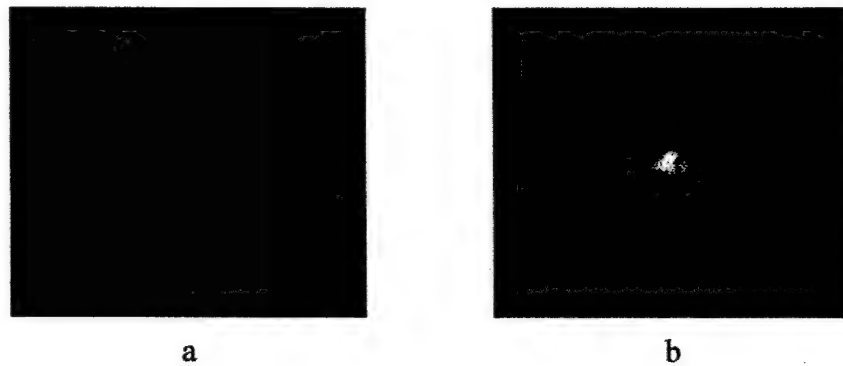


**Fig. 2.13.** Averaged intensity distributions in the focal plane F10 with the high-resolution adaptive system off and on (a and b, respectively) [5].

Figure 2.13 shows the averages of focal plane (F10) intensity distributions for the two cases: (a) the secondary loop is off, (b) the secondary loop is on. Each image was obtained by averaging 400 frames, which were recorded subsequently at 30 frames/s. The increased intensity in the center of Fig. 2.13 b illustrates the performance of the secondary loop. The experiments were performed on a rather hot summer day;  $C_n^2$  was about  $10^{-14} \text{ m}^{-2/3}$ . Fig. 2.14 shows the corresponding intensity profiles (averages of annular areas) for the two cases. The fiber diameter corresponds to about 15 pixels.

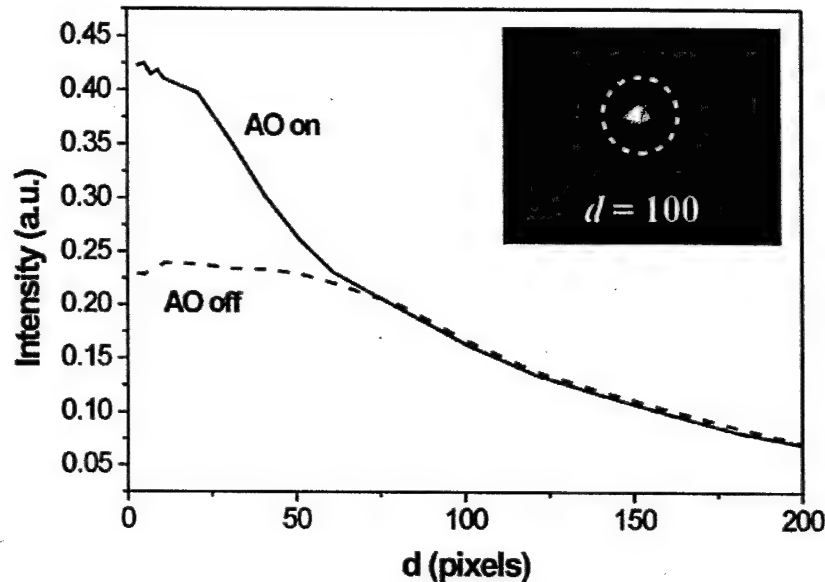


Fig. 2.14. Intensity profile in the focal plane with and without adaptation by the secondary loop ("AO on" and "AO off," respectively). The inset shows the focal plane image for "AO on" and a circle with 100 pixels diameter for scaling.

In conclusion, we built an adaptive optics system consisting of a beam-steering system as primary loop and a 132-control-channel adaptive optics system using a micro-machined deformable mirror controlled by the SPGD VLSI system as secondary loop. The system was tested with laboratory-generated turbulence and with an atmospheric propagation path. Although experimental circumstances were not very favorable for the latter experiments (the remote laser source was furnished with a diffuser to avoid beam steering), the presented first experiments demonstrated the improvement of the Strehl ratio after a 2.5 km atmospheric path in the case of rather strong turbulence with  $C_n^2 \approx 10^{-14} \text{ m}^{-2/3}$ .

### 2.3. References

1. T. Weyrauch, M.A. Vorontsov, T.G. Bifano, A. Tuantranont, V.M. Bright, J.R. Karpinsky, J.A. Hammer, "Performance evaluation of micromachined mirror arrays for adaptive optics", in *High-Resolution Wavefront Control: Methods, Devices, and Applications II*, J.D. Gonglewski, M.A. Vorontsov, and M.T. Gruneisen, Eds., Proc. SPIE 4124, p. 32-41 (2000).

1. T. Weyrauch, M.A. Vorontsov, T.G. Bifano, M.K. Giles, "Adaptive optics system with micromachined mirror array and stochastic gradient descent controller," in *High-Resolution Wavefront Control: Methods, Devices, and Applications II*, J.D. Gonglewski, M.A. Vorontsov, and M.T. Gruneisen, Eds., Proc. SPIE **4124**, p. 178-188 (2000).
2. T. Weyrauch, M.A. Vorontsov, T.G. Bifano, J. Hammer, M. Cohen, and G. Cauwenberghs, "Micro-scale adaptive optics: wavefront control with a  $\mu$ -mirror array and a VLSI stochastic gradient descent controller," *Appl. Opt.* **40**(24), 4243-4253 (2001).
3. T. Weyrauch and M.A. Vorontsov, "Dynamic wave-front distortion compensation with a 134-control-channel sub-millisecond adaptive system," *Opt. Lett.* **27**(9), 751-753 (2002).
4. T. Weyrauch, M.A. Vorontsov, and J. W. Gowens, "Adaptive compensation of atmospheric effects with a high-resolution micro-machined deformable mirror," in *High-Resolution Wavefront Control: Methods, Devices, and Applications IV*, J.D. Gonglewski, M.A. Vorontsov, and M.T. Gruneisen, Eds., Proc. SPIE **4825**, 14-23 (2002).

### 3. Experimental performance analysis of a high-resolution secondary wave front control loop

In an effort to improve the achievable Strehl ratio of Air Force closed-loop adaptive optics systems, the adaptive optics team at New Mexico State University (NMSU), in cooperation with researchers at the Army Research Laboratory's (ARL) Intelligent Optics Laboratory, is investigating concepts that utilize high-resolution LCSLM devices such as the array of microscopic liquid crystal phase modulators that make up a liquid crystal television (LCTV) panel to correct wave fronts that have been distorted due to propagation through the atmosphere. One concept that appears to be very promising utilizes a liquid crystal focal plane mask to generate a Zernike [1] filter and thus produce a phase-contrast irradiance image of the system pupil wherein the phase distribution in the pupil becomes an irradiance distribution in the image. Improved contrast of the phase-contrast image is obtained by forming two such images using  $\pm\pi/2$  Zernike filters. The irradiance information in these two phase-contrast pupil images is subtracted to form a differential phase-contrast image that is used to drive a high-resolution liquid crystal phase modulator so as to correct the input phase errors in the pupil. This paper follows closely an earlier theoretical paper on focal plane masks by Seward, et al [2]. Similar analysis is also found in recent papers by Vorontsov, Justh, et al [3,4]. Section 3.1 summarizes the basic theory of phase-contrast adaptive optics. Section 3.2 discusses the experimental setup of the optics and the electronic signals used to control the LCTV's, and sections 3.3 and 3.4 present the experimental results and conclusions.



### 3.1. Phase-Contrast Adaptive Optics—Basic Theory

#### 3.1.1. Wave front measurement

Figure 3.1 is a generalized unit magnification phase-contrast imaging system. Wave fronts passing through the telescope pupil are focused and thus Fourier transformed onto the image plane. The focused wave front is then Fourier transformed to form a new image of the pupil at the wave front sensor plane as shown. The differential Zernike filter is placed in the image plane so as to introduce a phase shift of  $\pm\pi/2$  to the zero-frequency Fourier component of the pupil function. The phase shift of the zero-frequency component causes the phase distribution in the pupil to be imaged as an irradiance distribution at the wave front sensor plane, thus allowing the phase to be visualized and measured. The mathematical basis is summarized in the next two subsections.

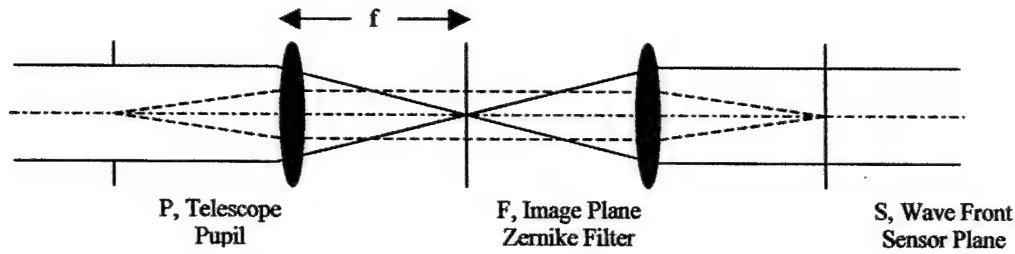


Figure 3.1. Simplified general layout for a phase-contrast Zernike filter using a unit magnification system.

#### 3.1.2. Simplified analysis for small pupil phase fluctuations in the pupil plane

The wave front at the pupil of the telescope can be expressed as

$$T(x,y) = P(x,y) \exp[j\phi(x,y)], \quad (3.1)$$

where  $P(x,y)$  is the field in the pupil plane in the absence of any phase fluctuations and  $\phi(x,y)$  represents the phase error in the pupil plane. For small phase fluctuations in the pupil,  $\phi(x,y)$  is very small, and Euler's law mathematically decomposes the exponential phase into two parts, a zero-frequency term and a term containing the higher spatial frequency fluctuations:

$$\exp[j\phi(x,y)] = \cos[\phi(x,y)] + j\sin[\phi(x,y)] \approx 1 + j\phi(x,y). \quad (3.2)$$

As the exponential phase function of equation (3.2) passes through a Zernike filter having a  $\pi/2$  phase shift at its center (zero frequency) and zero phase shift in the area surrounding its center, the constant term in equation (3.2) is multiplied by the complex exponential term,  $\exp(j\pi/2) = j$ . Therefore, the filtered exponential phase function becomes  $j[1 + \phi(x,y)]$ , and the resulting irradiance function at the wave front sensor plane contains the original pupil phase error,  $\phi(x,y)$ , as a measurable spatial fluctuation of the irradiance function.

$$E^+(x,y) = |P(x,y)|^2 |j[1 + \phi(x,y)]|^2 = |P(x,y)|^2 [1 + 2\phi(x,y) + \phi^2(x,y)] \approx |P(x,y)|^2 [1 + 2\phi(x,y)], \quad (3.3)$$

where, since  $\phi(x,y)$  is small,  $\phi^2(x,y)$  is insignificant.

Similarly, when the phase shift at the center of the Zernike filter described above is changed from  $\pi/2$  to  $-\pi/2$ , the constant term in equation (3.2) is multiplied by  $\exp(-j\pi/2) = -j$ , and the filtered phase function becomes  $j[\phi(x,y) - 1]$  so that the resulting irradiance function at the wave front sensor plane becomes

$$E^-(x,y) = |P(x,y)|^2 |j[\phi(x,y) - 1]|^2 = |P(x,y)|^2 [1 - 2\phi(x,y) + \phi^2(x,y)] \approx |P(x,y)|^2 [1 - 2\phi(x,y)]. \quad (3.4)$$

Subtracting the  $-\pi/2$  result from the  $+\pi/2$  result, we obtain the output of the differential Zernike filter:

$$E^+(x,y) - E^-(x,y) = 4\phi(x,y) |P(x,y)|^2. \quad (3.5)$$

The dynamic Zernike mask used in this experiment switches the central phase alternately between  $+\pi/2$  and  $-\pi/2$  every time  $\phi(x,y)$  is measured, and the dynamic differential signal used to calculate the phase error is the visibility function,

$$V = [E^+(x,y) - E^-(x,y)] / [E^+(x,y) + E^-(x,y)]. \quad (3.6)$$

For small pupil phase fluctuations,  $V = 2\phi(x,y)$ . Therefore, the values of  $\phi(x,y)$  are calculated directly from the value of  $V$  computed at every pixel. The metric of equation (3.6) allows for a calculation of the phase error that is independent of possible spatial fluctuations in the irradiance at the wave front sensor plane.

### 3.1.3. Large phase fluctuations in the pupil plane

For the general case of larger phase fluctuations, equation (3.7) from Born and Wolf [5], p. 427, gives the irradiance at the pupil image of a classical Zernike phase-contrast system as

$$E(x,y) = |C|^2 |P(x,y)|^2 [t^2 + 2\{1 - t\cos\alpha - \cos\phi(x,y) + t\cos(\alpha - \phi(x,y))\}], \quad (3.7)$$

where  $t$  is the amplitude transmission of the filter,  $\alpha$  is the phase shift at the center of the filter mask, and  $C$  is a constant that ensures conservation of energy. Equation (7) is derived in reference 2. For our system,  $t = 1$  and  $\alpha = \pm\pi/2$ . Therefore, for large phase fluctuations, equations (3.3), (3.4), (3.5), and (3.6) become [5]

$$E^+(x,y) = |C|^2 |P(x,y)|^2 [3 - 2\cos\phi(x,y) + 2\sin(\phi(x,y))], \quad (3.8)$$

$$E^-(x,y) = |C|^2 |P(x,y)|^2 [3 - 2\cos\phi(x,y) - 2\sin(\phi(x,y))] \quad (3.9)$$

$$E^+(x,y) - E^-(x,y) = |C|^2 |P(x,y)|^2 4\sin(\phi(x,y)), \quad (3.10)$$

and

$$V = 2\sin(\phi(x,y)) / [3 - 2\cos\phi(x,y)]. \quad (3.11)$$

#### 3.1.4. Wave front compensation

A frame grabber is used to grab the sequential  $\pm\pi/2$  phase-contrast images formed at the wave front sensor (plane S in Figure 3.1), and the pixel gray scales of the two images are used to calculate the differential irradiance visibility,  $V$ , given in equation (3.6), at every pixel. These values of  $V$  at every pixel are then converted to the corresponding gray scale levels needed to drive a LCTV phase screen and compensate the input phase errors,  $\phi(x,y)$ .

### 3.2. The Experiment

Although it was developed independently, the NMSU phase-contrast adaptive optics system is very similar to the wave front sensing and wave front control systems [3,4] developed by the Army Research Laboratory (ARL) in Adelphi, Maryland. The primary difference between the ARL and the NMSU experimental systems is found in the implementation of the liquid crystal focal plane mask. The ARL experimental mask is a nonlinear Zernike filter implemented using an optically-addressed liquid crystal light valve, while the NMSU experimental mask is a differential Zernike filter implemented using a phase-modulated pixilated LCTV panel. Figure 3.2 is a diagram of the high-resolution phase-contrast adaptive optics system that has been implemented using the NMSU High-Resolution Adaptive Optics Test Bed [6].

A helium neon laser beam enters the system at the bottom right and passes through a microscope objective/pinhole spatial filter to form a point source whose light is collimated by the first lens. The collimated beam illuminates the first LCTV (the system aperture stop) used as a phase screen to simulate atmospheric turbulence. The picture labeled "Input Phase" illustrates a typical phase distribution (rendered in gray scales) used for this purpose.

A two-lens 1:1 imaging system forms an image (a pupil plane) of the first LCTV at the location of the second LCTV which is used as the wave front corrector. Relay optics form another pupil image at the location of the wave front sensor camera (top left corner of Figure 3.2). The wave front sensor camera is used to visualize the spatially varying phase error introduced by the first LCTV phase screen as well as the residual phase error after the wave front correction loop (left side of Figure 3.2) is closed.

Five image planes (images of the point source) are formed by the system—two at the spatial filter locations, one at the science camera focal plane (upper right hand corner of Figure 3.2), one at the Zernike mask, and one at a diagnostic camera focal plane. The spatial filters, placed at the image planes between imaging lenses in both the bottom and middle legs of the system, filter the beam so as to remove the unwanted higher diffraction orders caused by the pixilated structure of the LCTV phase screens.

The science camera records the system point spread function (PSF) as the input and wave front corrector phase screens are changed and thus allows the changing PSF to be sampled and displayed in real time. The Zernike mask is a third LCTV used to implement the Zernike phase-contrast filter. It is placed at an image plane as shown.

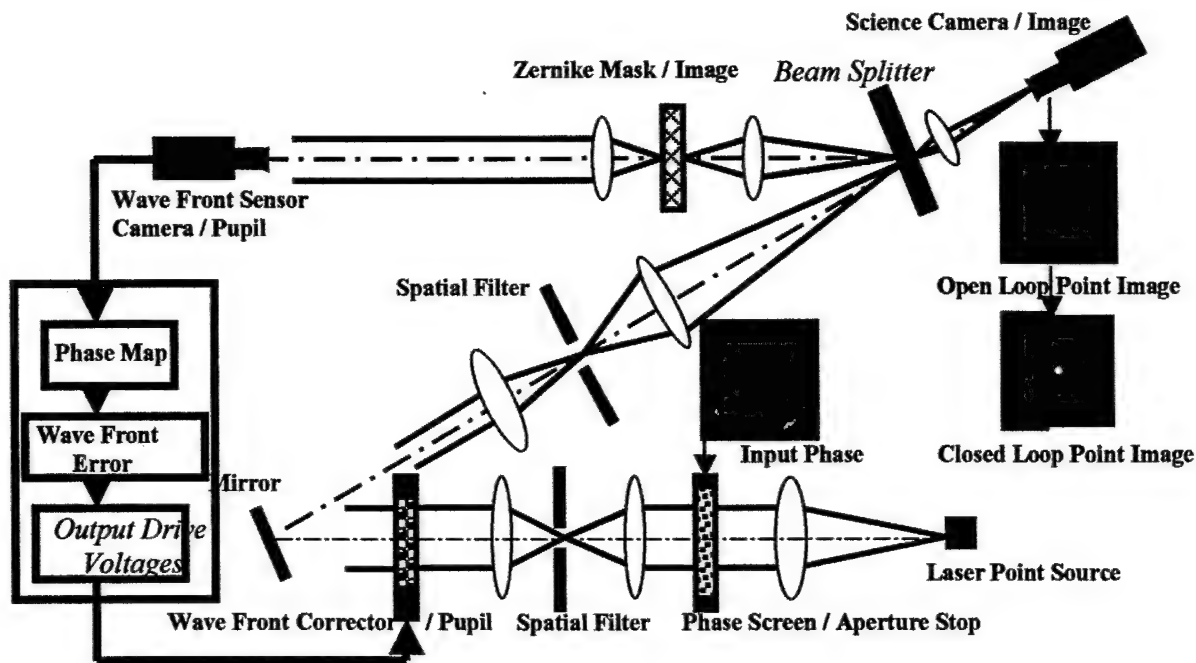


Figure 3.2. The phase-contrast adaptive optics system.

The final image plane (not shown in Figure 3.2) formed at the diagnostic camera is a magnified image of the focal plane mask that allows the structure of the mask to be seen superimposed on the system PSF in order to ensure that the PSF is adequately sampled by the pixilated LCTV mask. The system is designed with an  $F/\#$  large enough to produce an ideal diffraction-limited Airy disk at the mask that is wide enough to be sampled by at least two pixels in each dimension. This ensures there will be no aliasing in the final pupil plane recorded by the wave front sensor camera. Figure 3.3 is an example phase-contrast image. Note that the spatially replicated images of the aperture stop in the final pupil plane do not overlap, indicating that the PSF is adequately sampled. Only the central, zero-order phase-contrast pupil function is sent to the computer and used to compute the feedback signal (equation (3.11)) used to drive the wave front corrector.



Figure 3.3. A phase-contrast image.

### 3.4. Results

The phase-contrast adaptive optics system works very well for correcting simulated static turbulence patterns. It has also been used successfully to correct simulated dynamic turbulence. Figure 3.4 a presents a simulated static residual phase pattern representative of the residual phase in a telescope pupil after correction using a primary adaptive optics loop with a deformable mirror. Figure 3.4 b is the system psf obtained using the NMSU high-resolution system with the residual phase of Figure 3.4 a written on the input phase screen, and Figure 3.4 c is the resulting system psf after compensation using the high-resolution phase-contrast adaptive optics system.

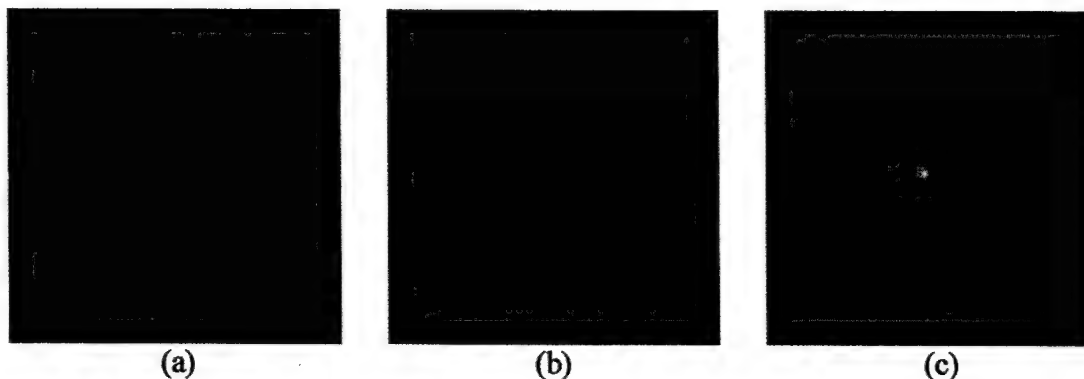


Figure 3.4. Results obtained using the high-resolution phase-contrast adaptive optics system with a static residual phase in the input phase screen: (a) input phase (gray levels 0-250 represent phase  $0-2\pi$ ), (b) degraded psf at the science camera, (c) compensated psf.

Figure 3.5 shows one frame from an input sequence that simulates atmospheric turbulence. Figures 3.6 a and 3.6 b present the initial degraded psf and the final compensated psf obtained from a dynamic sequence of simulated phase patterns similar to that shown in Figure 3.5.

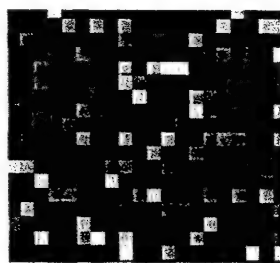


Figure 3.5. One frame of simulated turbulence written to the input phase screen.

There are at least two metrics that can be used to determine the effectiveness of the closed-loop compensation—psf peak irradiance and psf spot size. As the adaptive algorithm proceeds, the energy in the sidelobes of the degraded psf move into the center, causing the overall spot size to decrease and the peak irradiance to increase. In this dynamic experiment, a simulated phase screen with Kolmogorov statistics was translated



across the first LCTV (the system aperture stop shown in Figure 3.2). The frame in Figure 3.5 is just one small portion of the moving turbulence phase screen, and Figure 3.6 b is the compensated psf obtained by closing the adaptive loop while that portion of the phase screen was present on the input LCTV. As the phase screen data was scrolled, frame by frame, across the input LCTV, the compensated psf was recorded and analyzed for each frame. Figure 3.7 presents the results obtained by analyzing a sequence of ninety frames with the adaptive loop open and closed. For each frame, the spot is fitted to a Gaussian, the standard deviation of the spot is computed (in pixels), and the inverse of the standard deviation is plotted in Figure 3.7. Thus, a smaller spot size yields a larger value of the metric (inverse of standard deviation) in the plots. The upper trace in Figure 3.7 plots the inverse spot size (inverse of the standard deviation) for the closed-loop system, and the lower trace plots the same metric for the open-loop system (without correction). Although there is a lot of variation in the metric due to the changing turbulence, the data show that the adaptive system works dynamically to reduce the size of the system psf.

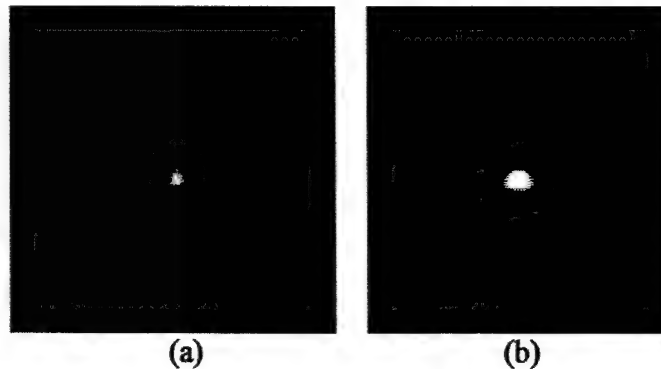


Figure 3.6. Results obtained from the phase-contrast adaptive optics system for one frame of a dynamic sequence of simulated input turbulence: (a) initial degraded psf, (b) compensated psf for a single frame.

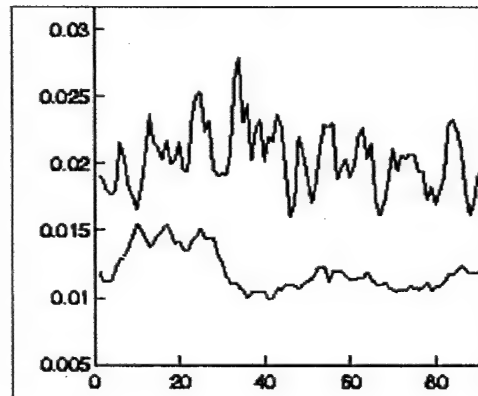


Figure 3.7. Plots of the metric (inverse of the psf standard deviation) for a sequence of ninety frames of simulated turbulence. The lower trace plots the metric for the open-loop system and the upper trace for the closed-loop system.

In conclusion, a closed-loop adaptive optics system that uses a differential phase-contrast focal plane filter has been implemented successfully at NMSU. The differential filter is implemented using an electrically-addressed liquid-crystal spatial light modulator (LCSLM) operated in a phase-mostly mode. Preliminary experimental results indicate that the system works well as it automatically compensates both static and dynamic input phase errors.

### 3.6. References

1. F. Zernike, "How I discovered phase contrast," *Science* **121**, 345-349 (1955).
2. A. Seward, F. Lacombe, and M. K. Giles, "Focal plane masks in adaptive optics systems," *Proc. SPIE* **3762**, 283-293 (1999).
3. M. A. Vorontsov, E. W. Justh, and L. A. Beresnev, "Adaptive optics with advanced phase-contrast techniques. I. High-resolution wave-front sensing," *J. Opt. Soc. Am. A* **18**, 1289-1299 (2001).
4. E. W. Justh, M. A. Vorontsov, G. W. Carhart, L. A. Beresnev, and P. S. Krishnaprasad, "Adaptive optics with advanced phase-contrast techniques. II. High-resolution wave-front control," *J. Opt. Soc. Am. A* **18**, 1300-1311 (2001).
5. M. Born and E. Wolf, *Principles of Optics*, Pergamon Press, Oxford, sixth ed., 1980.
6. M. K. Giles, A. Seward, M. A. Vorontsov, J. Rha, and R. Jimenez, "Setting up a liquid crystal phase screen to simulate atmospheric turbulence," *Proc. SPIE* **4124**, 89-97 (2000).

### 4. Experimental performance analysis of a reconfigurable Shack-Hartmann wave front sensor (RSH) using a dynamic lenslet array written on a projector LCD.

The conventional Shack-Hartmann wave front sensor (SHS) has a fixed subaperture size that sets (1) the amount of light that can be collected by each subaperture, and (2) the maximum wave front error that can be detected without ambiguity. The subaperture size also determines the number of subapertures that fit in the pupil and therefore the spatial resolution of the wave front measurements. Obviously, a tradeoff is made in the design of the wave front sensor, and the subaperture size is chosen based on some nominal average seeing condition. If the strength of turbulence exceeds the nominal design condition, the sensor can no longer make accurate wave front measurements because (1) the amount of light collected by each subaperture (and the corresponding spot irradiance) is too small to detect or (2) the wave front slope is so large that the spot moves out of the position measurement region of the subaperture. In the latter case, the spot either moves into the region of an adjacent subaperture causing an ambiguity or it moves into a guard band region between subapertures designed to avoid such ambiguities and is not detected.

We present a reconfigurable Shack-Hartmann wave front sensor (RSH) with a dynamic reconfigurable array of lenses written on a phase-modulated, twisted nematic

liquid crystal display module (LCD). This sensor can improve the performance of wave front control systems used in adaptive optical telescope applications by enabling the sensor to measure the wave front slope even in poor seeing conditions. Existing SHS systems typically increase the integration time to collect more photons as the input irradiance decreases, thus enabling continued (albeit degraded) operation of the wave front control system. The RSH maintains the same integration time (and bandwidth) but increases the subaperture size to collect more photons and accomplish the same purpose. In section 4.1 we show that this increase in spatial integration produces a significantly smaller residual error than an equivalent increase in the integration time. Suppose, for example, that the sensor is working with a standard subaperture size when an increase in scintillation causes the Hartmann spot irradiance to drop below the threshold of detection. In such a situation, the RSH monitors the spot irradiance and automatically increases the subaperture size to collect more light and thus increase the spot irradiance, enabling the system to continue its operation, albeit with reduced spatial resolution. Similarly, the adaptive sensor, which uses a high-resolution CCD to measure the spot centroids, can monitor the spot positions and automatically increase the size of the appropriate subapertures whenever spots begin to move into adjacent regions.

This reconfigurable sensor can also improve the quality of the wave front measurements in the following manner. Guard bands used between subapertures to avoid measurement ambiguities can cause gaps in the measured wave front. The dynamic array of lenses can be shifted back and forth between measurements to fill in the gaps, thus producing a more complete and accurate measurement of the entire wave front. Section 4.2 presents the design and layout of the RSH, and section 4.3 presents experimental results using the RSH in the presence of simulated Kolmogorov turbulence and under conditions of changing irradiance.

#### 4.1. Residual wave front errors due to increasing spatial and temporal integration

The performance of an adaptive optics system is dependent on a variety of conditions and parameters. Tyson presents a comprehensive list and discussion of the various errors encountered by adaptive optic systems [1]. Three fundamental aspects of a system are the temporal response, the wave front spatial sampling, and the wave front sensing radiometric performance. For an astronomical system that uses a Hartmann wave front sensor and a zonal deformable mirror, and assuming Kolmogorov atmospheric statistics, the wave front correction variance due to finite temporal response is,

$$\sigma_{temp}^2 = \left( \frac{f_o}{f_c} \right)^{5/3} \quad (4.1)$$

where  $f_o$  is the atmospheric Greenwood frequency and  $f_c$  is the system closed-loop cutoff frequency. The cutoff frequency is inversely related to the integration time,  $\Delta t$ , of the wave front sensor,

$$f_c = \frac{1}{N\Delta t} \quad (4.2)$$

where  $N$  is a factor that depends on the efficiency of the closed-loop system. Sampling theory requires that  $N$  have a value of at least 2. In practice,  $N$  is often as large as 10. The spatial sampling/fitting error variance is given by,

$$\sigma_{fit}^2 = \kappa \left( \frac{r_s}{r_o} \right)^{5/3} \quad (4.3)$$

where  $r_o$  is the atmospheric coherence diameter,  $r_s$  is the effective distance between deformable mirror actuators at the entrance pupil, and  $\kappa$  is an influence function parameter that ranges in value from 0.23 for a Gaussian actuator influence to 1.26 for piston-only influence. In practice,  $r_s$  is also typically equal to the length of a wave front sensor subaperture zone. The wave front variance due to wave front sensor radiometric signal-to-noise ratio,  $SNR$ , can be described by,

$$\sigma_{WFS}^2 = \rho \frac{\pi^2}{4 \cdot SNR^2} \quad (4.4)$$

where  $\rho$  is a parameter that depends on the Hartmann spot sensing approach. For a quad-cell,  $\rho = 0.35$ .

Any of the three errors described by Eqs. (4.1), (4.3), and (4.4) could dominate the corrected wave front result depending on conditions in which the system is operating. If we consider the situation where low-light on the wave front sensor is of primary concern, then there are essentially two approaches for improving the wave front sensing signal-to-noise ratio: A) increase the wave front sensor integration time, or B) increase the collection area of each subaperture in the wave front sensor. Both options reduce the error described in Eq. (4). However, on the downside, Option A also increases the error in Eq. (4.1) and Option B increases the error described by Eq. (4.3).

Typically, Option A is carried out in low-light situations since changing control bandwidth is usually a simple matter of changing wave front sensor frame rate and control loop constants [2]. However, a cursory examination of Eqs. (4.1) and (4.3) suggests that Option B, increasing the subaperture size, may actually be preferred in many situations with regard to minimizing total wave front error. Consider Eq. (4.3): the fitting variance increases as the subaperture spacing ( $r_s$ ) to the 5/3-power whereas the number of photons collected increases as roughly the spacing *squared* (with the *area* of the subaperture). So as the subaperture size is increased, the fitting variance will increase as the number of photons collected to the 5/6-power. Now consider Eqs. (4.1) and (4.2): the temporal wave front variance increases as the integration time ( $\Delta t$ ) to the 5/3-power, which is an analogous situation to the fitting error dependence on  $r_s$ . However, in this case the number of photons collected simply increases *linearly* with integration time. Thus, for increasing integration time, the temporal error variance will increase as the number of photons collected to the 5/3-power. So assuming, for example, that the temporal and spatial error variances are of similar value initially, then changing the subaperture size to reach a given photon flux will follow a square root better correction performance course than leaving the subaperture size fixed and increasing the integration time.

In practice, the variance terms in Eqs. (4.1), (4.3), and (4.4) are coupled through radiometry and it turns out that an optimal combination of control bandwidth and subaperture size can be found for specific conditions. This concept can be illustrated by evaluating Eqs. (4.1) through (4.4) in a simple example analysis. For the wave front sensor, we assume a fast-framing CCD camera where the radiometric SNR is given by [3],

$$SNR = \frac{\eta \phi \Delta t}{\sqrt{\eta \phi \Delta t + N_{pix} \sigma_r^2}} \quad (4.5)$$

where  $\eta$  is the CCD quantum efficiency,  $N_{pix}$  is the number of pixels that lie under a subaperture lenslet spot, and  $\sigma_r$  is the read noise per pixel. The photon flux per subaperture,  $\phi$  (photons/sec) is,

$$\phi = E_q r_s^2 T_r \quad (4.6)$$

where  $E_q$  is the irradiance (photons/sec-cm<sup>2</sup>) at the system entrance pupil and  $T_r$  is the transmission to the CCD sensor. The performance measure we assume for the analysis is the Strehl ratio, where it is given by the approximation [1],

$$S = \exp\left\{-\left(\sigma_{temp}^2 + \sigma_{fit}^2 + \sigma_{WFS}^2\right)\right\} \quad (4.7)$$

The parameter values for our example are listed in Table 4.1. The values are typical for a visible light system. The photon irradiance value,  $E_q$ , is approximately that expected for a 8<sup>th</sup> visual magnitude star of temperature 5900 K and sensing over wavelengths from 0.4 to 0.7  $\mu$ m. The remaining two free parameters for the analysis are the subaperture length (actuator spacing),  $r_s$ , and the integration time,  $\Delta t$ . The curves presented in Fig. 4.1 show the resulting Strehl value as a function of subaperture length for several integration times.

Table 4.1. Parameter values for adaptive optic system performance example.

$00f_o$	<i>Atmosphere Greenwood frequency</i>	30 Hz
N	Closed-loop control scaling factor	10
$\kappa$	Mirror influence function	0.36
$r_o$	Atmosphere coherence diameter	5 cm
$\rho$	Wave front sensor scaling parameter	0.35
$\eta$	<i>CCD quantum efficiency</i>	0.8
$N_{pix}$	<i>Pixels under lenslet spot</i>	4

$\sigma_r$	Pixel read noise	5 e <sup>-</sup>
$T_r$	Wave front sensor optical transmission	0.5
$E_q$	Photon irradiance at entrance pupil	$1.84 \cdot 10^3$ photons/s- cm <sup>2</sup>

The most-favorable operating point shown in Fig. 4.1 is a Strehl value of about 0.47 with  $r_s \approx 6$  cm and  $\Delta t = 1$  msec. Significantly increasing or decreasing either  $r_s$  or  $\Delta t$  results in poorer performance. Now consider the situation if we had a system designed with a fixed subaperture size of 10 cm (perhaps because 10 cm coherence diameters were common at our observatory). Given the 5 cm seeing case of Fig. 4.1, it is apparent there is no integration time that will provide the peak possible Strehl. The best we could hope for is a Strehl of about 0.29. So clearly, the ability to reconfigure the subaperture area, in combination with control bandwidth adjustment, provides superior performance over a system with fixed subaperture area in cases where the coherence diameter is different than the design point.

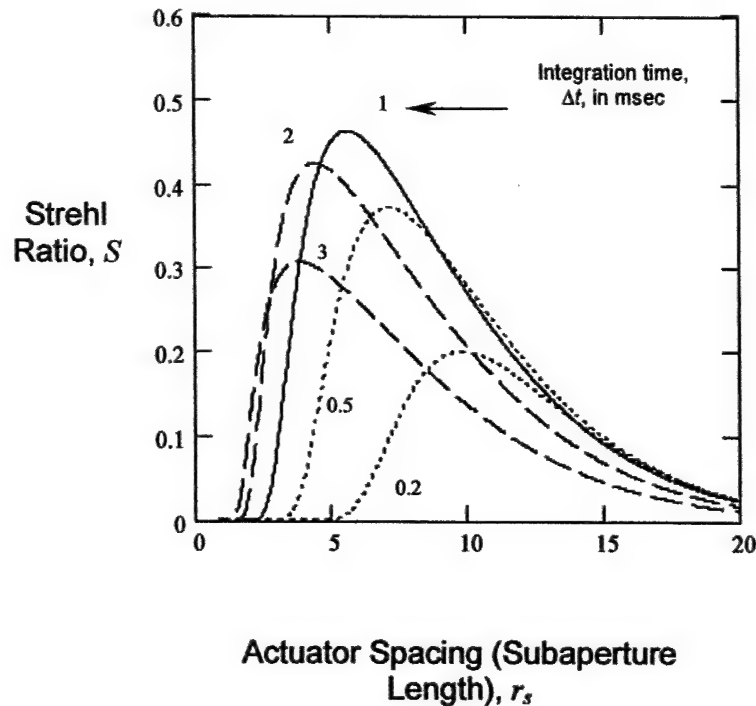


Figure 4.1. Strehl ratio as a function of actuator spacing,  $r_s$ , for a range of sensor integration times,  $\Delta t$ .

#### 4.2. Set Up for the Reconfigurable Shack-Hartmann Wave Front Sensor

Several researchers have demonstrated Fresnel lenses and lens arrays written on LCD devices operating in binary-phase [4,5] and continuous-phase [6,7] modes. We have developed a reconfigurable Shack-Hartmann wave front sensor similar to the one suggested by N. Clark [4], but using continuous-phase instead of amplitude coupled with binary-phase modulation. Figure 4.2 shows the set up used to demonstrate the operation of our reconfigurable Shack-Hartmann wave front sensor. The dynamic lenses developed for the reconfigurable Shack-Hartmann wave front sensor are encoded as sampled continuous-phase Fresnel lens functions written to the pixels of a twisted nematic LCD module (LCD 3 in Figure 4.2) operating in a continuous phase-mostly mode [8]. The sampled continuous Fresnel lens phase functions convert the local tilted plane waves at the subapertures to an array of converging spherical waves that focus to form an array of Hartmann spots that is imaged to fit the size of CCD 2 using a relay lens as shown at the bottom of Figure 4.2. The system point spread function (PSF) is monitored using CCD 1, shown on the right side of Figure 4.2.

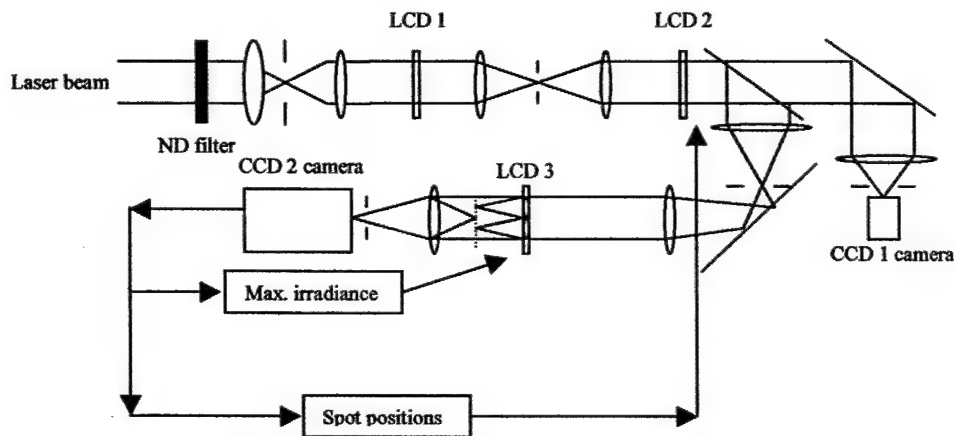


Figure 4.2. Reconfigurable system setup.

LCD 1 in Figure 4.2 is used to generate an input wave front composed of an array of truncated plane waves, each of which is tilted differently with a size large enough to cover its corresponding subaperture (Fresnel lens). As the tilts of the individual truncated plane waves change, the focal spots move. The spot positions, obtained from the CCD 2 data using a conventional centroid algorithm, are used to compute the average input wave front tilts at all subapertures and to generate a compensating wave front on LCD 2 as indicated by the spot positions arrow in Figure 4.2.

To demonstrate the ability of the sensor to adapt to changing input amplitudes, we placed a rotating variable neutral density filter (ND filter) in the input laser beam as shown in Figure 4.2. Starting with a simple 4x4 array of Hartmann lenses, we operated the system at full amplitude and allowed it to automatically measure the positions of the 16 spots. With the system running, we rotated the ND filter, causing the peak spot irradiance values to decrease until they fell below the threshold of detection, at which point the system automatically changed from a 4x4 array to a 2x2 array of lenses in order



to collect more power in each Hartmann spot, thus enabling the wave front sensor to continue operating with reduced resolution at lower light levels.

### 4.3. Experimental Results

In this experiment, Kolmogorov turbulence is used as a sample turbulence screen that is placed in LCD 1 as shown in Figure 4.2. Figure 4.3 shows the experimental results. The static Kolmogorov turbulence screen shown in Figure 4.3 a is defined with a peak-valley value of  $2\pi$  and a  $D/r_0$  of 6 where  $D$  is the entrance pupil diameter and  $r_0$  is the Fried diameter. The system entrance pupil contains the central  $96 \times 96$  pixels of the screen. The point spread function (PSF) of this system is degraded as shown in Figure 4.3 b due to the turbulence. Figure 4.3 shows experiment result. Figure 4.3 d shows the corrected PSF obtained using the reconstructed wave front shown in Figure 4.3 c, generated using a zonal fitting algorithm. There are some residual errors due to imperfect optical components.

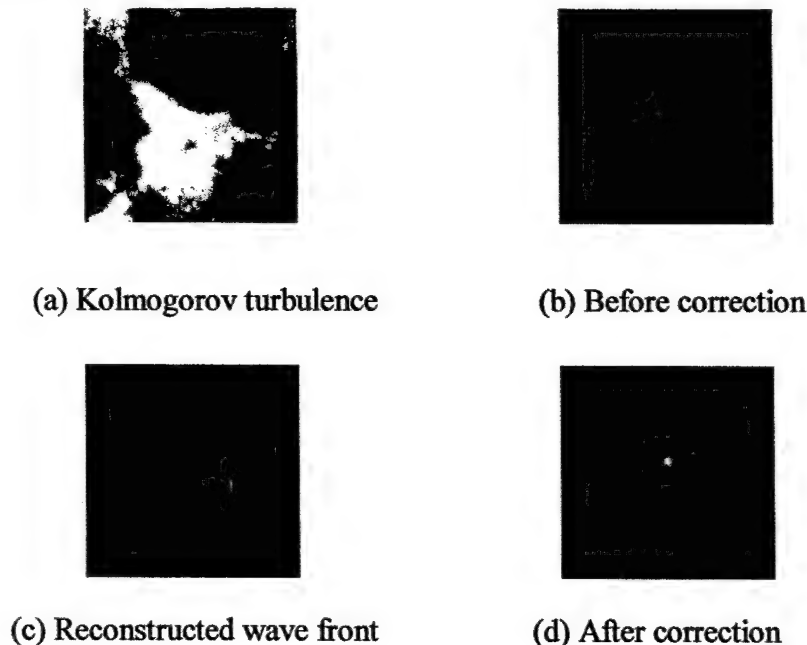


Figure 4.3. Reconstructed wave front with Kolmogorov turbulence.

Figure 4.4 illustrates the dynamic adaptation (reconfiguration of the array of lenses) realized using the reconfigurable Shack-Hartmann sensor. When the light level is reduced (perhaps by scintillation) the Hartmann focal spots become very dim, and the conventional centroid program has trouble finding the spot locations. Therefore, in order to increase the irradiance of each focal spot, the system automatically writes fewer larger lenses with the same focal length, thus decreasing the  $F\#$  of the lenses and increasing the spot irradiance. Figures 4.4 a and 4.4 b show a  $4 \times 4$  array of Hartmann spots before and after the decrease in light level. Figure 4.4 c shows the  $2 \times 2$  array of Hartmann spots produced after the sensor adapts to the lower light level.



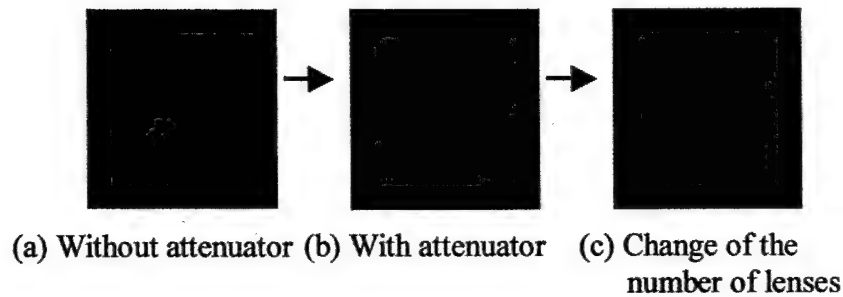


Figure 4.4. System automatic reconfiguration.

In conclusion, the reconfigurable Shack-Hartmann sensor works has been tested under low light level conditions at NMSU. The tests indicate that the system works very well and that it is a superior alternative to existing systems that increase the system integration time in order to operate under low light level conditions.

#### 4.4. References

1. R. K. Tyson, *Principles of Adaptive Optics*, 2<sup>nd</sup> edition (Academic Press, 1998).
2. L. C. Roberts and C. R. Neyman, "Characterization of the AEOS Adaptive Optics System," *Pub. Astron. Soc. Pac.* 114, 1260-1266, 2002.
3. R. D. Fiete and T. Tantaló, "Comparison of SNR image quality metrics for remote sensing systems," *Opt. Eng.* 40, 574-585, 2001.
4. N. Clark, "Spatial light modulator having amplitude coupled with binary phase mode," U.S. Patent Number 5,535,029, July 9, 1996.
5. D. M. Cottrell, J. A. Davis, T. R. Hedmann, and R. A. Lilly, "Multiple imaging phase-encoded optical elements written on programmable spatial light modulators," *Appl. Opt.* 29, 2505-2509 (1990).
6. Vincent Laude, "Twisted-nematic liquid-crystal pixilated active lens," *Optics Communications* 153, 134-152 (1998).
7. Rensheng Dou, "Wavefront control using a liquid crystal television," Ph.D Dissertation, New Mexico State University, Chapter 4, (May, 1996).
8. Narasimha S. Prasad, Sean M. Doyle, and Michael K. Giles, "Collimation and beam alignment: testing and estimation using liquid-crystal televisions," *Opt. Engrg*, 35, 1815-1819 (July 1996).

## **5. Controlling a laser beam in the presence of strong turbulence.**

### **5.1. Introduction**

Michigan Technological University (MTU) supported this program in two ways: (1) we examined extending the image sharpness metric approach developed by Mikhail Vorontsov to control the deformable mirror in a laser beam projection system operating under conditions of saturated scintillation; and (2) we supported investigators at New Mexico State University by providing some simulated phase screens to use in their efforts. Much of this work has been devoted to the problem of controlling a laser beam in the presence of strong turbulence.

Many laser projection systems, such as those found in laser weapon systems and laser communication systems, have the goal of focusing a laser beam on a target through a long atmospheric path. The objective of these systems is often to concentrate as much power as possible on a small area of the target. In long range air-to-air laser projection systems, the laser beam must propagate almost horizontally through atmospheric turbulence. In the absence of atmospheric turbulence, the beam reaching the target would have a high power density and an almost Airy-disk pattern as predicted by diffraction theory. However, in conditions of strong atmospheric turbulence, the amplitude and phase of the laser beam are severely distorted as the beam propagates through the long optical path. Therefore the beam reaching the target in general has a low power density, and its intensity pattern is randomly changing and speckled in appearance.

A laser beacon-based adaptive optics system provides a way to correct for the turbulence-induced phase distortion. In this system, a beacon is created by transmitting one or more low power laser beams from the laser projection system to the target. Some of the light from the beacon scatters back through the atmosphere and is captured by the aperture of the laser projection system. Assuming that all the sources of the scattered light captured by the aperture of the laser projection system emanate from a very small region of the target, conventional adaptive optics systems can lead to a significant improvement in performance. Ideally, to compensate for weak phase distortions, the conjugate of the phase of the beacon field incident on the aperture is applied to the outgoing beam. In practice, the phase conjugation is performed by controlling the shape of a reflective deformable mirror. The deformable mirror is in turn controlled through a set of actuator control weights obtained processing either wave front sensor information, image information, or both. Assuming weak turbulence, and that the outgoing laser beam propagates through roughly the same optical path as the scattered light, the beam reaching the target will approach diffraction-limited performance.

Unfortunately, the approach described above works well only in cases where the atmospheric turbulence is weak and the beacon is a point source. In beam projection systems operating in conditions of strong atmospheric turbulence, the amplitude and phase of the field incident on the target are severely distorted, and the target itself is extended. Therefore, the beacon that is created is not a point source, but rather it is a randomly shaped, extended source. Because the beacon field is scattered by an optically rough surface, the beacon is also spatially incoherent. Hence, in most cases of practical interest the beacon subtends an angle that is many times larger than the isoplanatic angle so that the beacon looks like a collection of several small isoplanatic patch-sized regions. The scattered light from each one of these regions goes through a slightly different volume of turbulence and experiences different amplitude and phase distortions. Hence

the field incident on the aperture originates from different isoplanatic patch-sized regions of the beacon, and this total field causes the image and Hartman sensor data we would measure. The various random point spread functions arising from different parts of the beacon are super-imposed in both the image and Hartman sensor data. Simply conjugating the phase estimated from the Hartman sensor and image data, and applying it to the outgoing laser beam is not as effective as finding a means to isolate and conjugate the phase associated with a small patch on the target. The approach we describe later in this paper provides a way to reduce the errors related to what we call "beacon anisoplanatism". In addition to the anisoplanatism described above, the beacon field experiences strong scintillation because of the long optical paths through which it propagates. However, the approach described in this paper is a phase conjugation scheme and does not compensate for amplitude errors. However, we will show that phase-only correction is still useful.

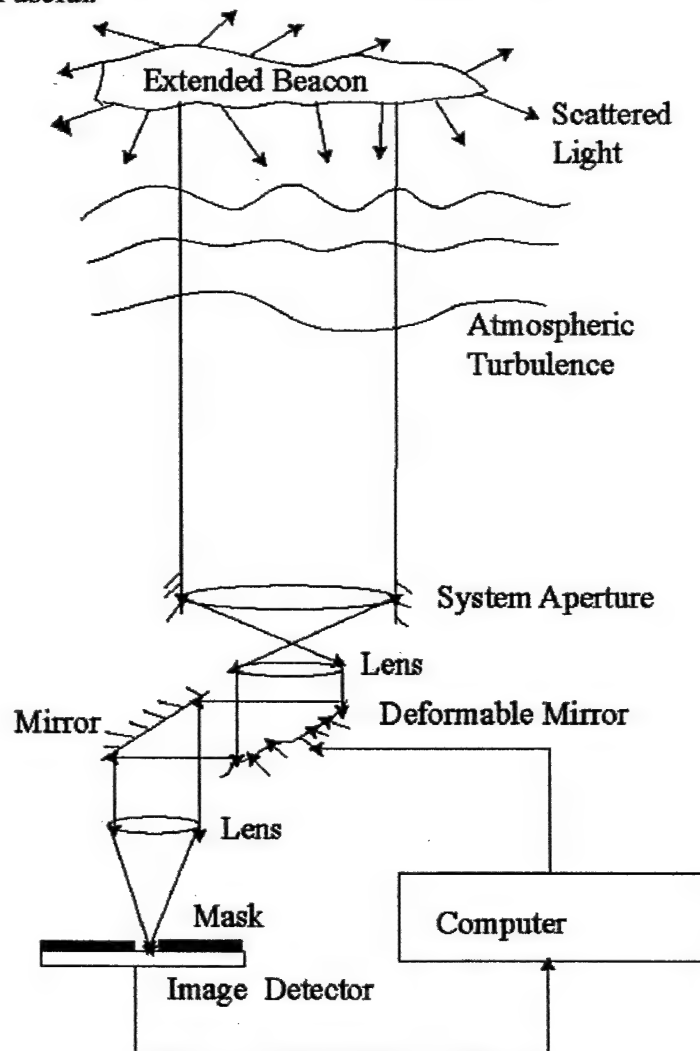


Figure 5.1. Schematic representation of the image sharpness metric-based approach.

Most previous work in this area has involved the use of the entire scattered field incident on the aperture in order to find the optimum control weights to apply to the

deformable mirror. For instance, Roggemann et al. described a nonlinear optimization-based technique to determine the deformable mirror figure which jointly processes Hartman sensor and image data to obtain commands for a deformable mirror. We have found that his approach provides only small improvements in percentage of encircled energy when the beacon is extended, and is very computationally intensive. Here, we describe an approach that is based on a modified version of the laser beacon and phase-conjugation adaptive optics system. As shown in Figure 5.1, instead of using all the scattered light from the beacon, we have developed a measurement and processing technique that seeks to use a small portion of the light emanating from a small patch on the beacon. This patch subtends an angle that is only a few times larger than the isoplanatic angle and forms the basis for the image sharpness metric. The image sharpness metric used here was first described by Muller and Buffington et al, and was later used by Voronstov, et al. This image sharpness metric is given by

$$J(\alpha) = \int M(x) I(x, \alpha) d^2x$$

where  $x$  is the position vector in the image plane,  $M(x)$  is a binary mask which blocks the light from some regions of the image plane,  $I(x)$  is the image intensity due to the beacon, and the  $\alpha$ 's are the DM actuator commands. As we mentioned above, the image intensity contains components from several isoplanatic patch-sized regions. Therefore a spatial filter, in this case the mask,  $M(x)$ , with a small circular aperture is used as a field stop to pass only light from a small region of the target to the optimization metric. If the diameter of the mask aperture subtends an angle that is a few times larger than the isoplanatic angle, we can effectively compensate for an almost isoplanatic patch-sized portion of the target by iterating on the elements of  $\alpha$ . The deformable mirror then performs the necessary phase correction to the outgoing high power laser. Several optimization algorithms such as the BFGS quasi-Newton method and the simultaneous perturbation stochastic approximation (SPSA) can be used to find the optimum values of  $\alpha$  that maximize the image sharpness metric,  $J(\alpha)$ . However, we used the SPSA because of its convergence speed.

So far the results obtained with this approach have been promising. The results from our simulations show that deformable mirror control based on the nonlinear optimization of the image sharpness metric, leads to an improvement in the percentage of encircled energy over previous DM control approaches based on simply conjugating the phase obtained from wavefront sensors and reconstructors. The simulation results also show that ideal mask aperture can subtend an angle that is many times larger than the isoplanatic angle. However as the turbulence strength increases, the size of the mask aperture must also be increased. The simulation results show that in some cases the best angular subtense can be many times the isoplanatic angle.

## 5.2. Image Sharpness Metric-Based Approach

In cases of interest to us, the angular extent of the beacon is many times larger than the isoplanatic angle. Therefore at the aperture, the beacon looks like a collection of many isoplanatic patch-sized sources. To reduce anisoplanatism we have to pick a patch on the beacon that is on the order of the size of the isoplanatic patch, and try to estimate

the impulse response due to atmospheric propagation for light emanating from that point. We do this by filtering out some of the light from the other isoplanatic patch-sized sources in the beacon by using a mask in the image plane which acts as a field stop. Figure 5.2 shows the relationship between the angular subtense,  $\theta_{\text{mask}}$ , and the diameter of the mask's aperture. Our approach is to iterate on the DM commands (DM not shown in Fig. 5.2) to maximize the intensity encircled by the mask. The resulting phase profile is applied to the outgoing beam, which is propagated back to the target

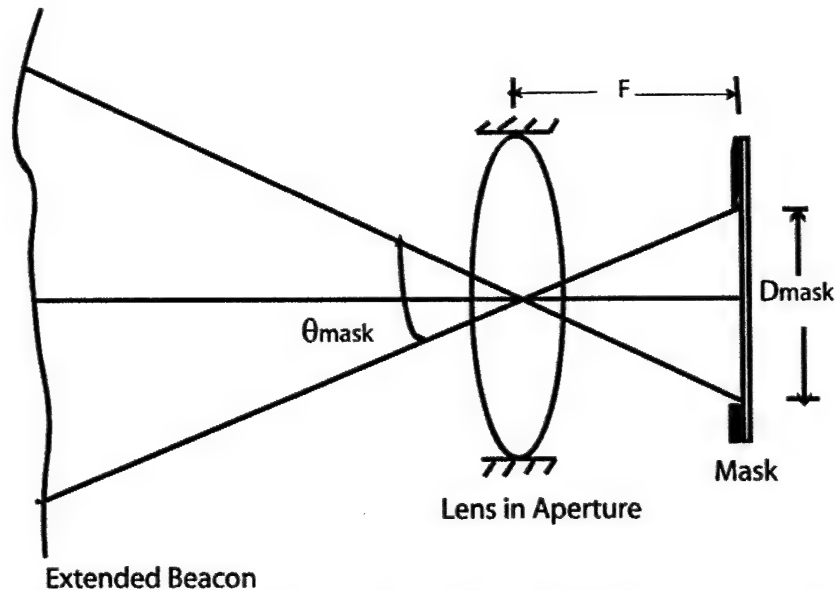


Figure 5.2. Illustration of the relationship between the mask and the patch subtended on the extended beacon.

Analytical solutions to the propagation of laser projection systems under conditions of strong atmospheric turbulence are not available at this time. Therefore, we used the Monte Carlo method to simulate several independent optical propagations. The percentage of encircled energy in the ensemble average target intensity is used as the performance metric. Each simulation can be broken down into several parts. The first part is the creation of the extended beacon of wavelength,  $\lambda = 980 \text{ nm}$ . The second part is the propagation of the scattered extended beacon wave fronts from the target plane to the aperture of the laser beam projection system. In the next part we form an image of the field in the system aperture and then optimize the image sharpness metric described above. Finally, we correct the phase of the outgoing high power laser beam.

The extended beacon was created by propagating a gaussian beam to a target at a simulated distance of 50 km. In our simulations, the target plane was created on a  $1024 \times 1024$  uniform Cartesian grid. In the simulations, we used a 5-layered atmospheric model. The 5 thin layers were uniformly spaced so that the distance between each thin layer was 10 km. The first layer was placed at a distance of 10 km from the beacon plane and the last layer was placed in the laser projection system's aperture plane. Each layer (or phase screen) was created using a phase screen generator. In turn the phase screen was created on a  $1024 \times 1024$  Cartesian grid with a sample spacing of 0.568 cm. Each phase screen had a von Karman power spectral density, with outer scale of 10 m, and an

inner scale of approximately zero. We assumed that each phase screen had the same structure constant of the index of refraction  $C_n^2$ . Furthermore,  $C_n^2$  was independent of position and was therefore a constant. The isoplanatic angle,  $\theta_0$ , and the Fried parameter,  $r_0$ , changed depending on the structure constant.

To simulate scattering, the central portion of the field at the target was extracted by modeling the target as a 0.5 m diameter circular Lambertian scatterer. It was then propagated in the reverse direction back to the laser projection system's receiver. The propagation was through the same turbulent volume that the previous gaussian beam had traversed. The aperture diameter of the laser projection system was 1.0 meter.

An ideal lens in the system aperture was used to form an image of the incoming wave front. This far-field image was created by performing a FFT of the field just after the ideal lens. We used the image sharpness metric as the objective function and maximized it by finding the optimum set of  $\alpha$ 's. The optimization algorithm used in this case was the SPSA algorithm. We chose to use the SPSA algorithm because it converged much faster than the BFGS quasi-Newton algorithm. The optimum  $\alpha$ 's are used to drive the deformable mirror and hence create to optimum phase correction. The size of the circular hole was varied to get the best results.

Finally, the optimum corrected phase is applied to the outgoing high power laser beam using a simulated DM model. This beam propagates through the same turbulent volume as the scattered light until it reaches the target plane. The intensity at the target plane is saved so that it can be used in the calculation of the percentage of encircled energy. We performed several independent realizations. Then we added the intensities in the target plane for each one of the realizations and calculated their ensemble average intensity. Next we compute the percentage of encircled energy from the ensemble average intensity. We used the percentage of encircled energy to measure the quality of the target image.

### 5.3. Results

We now present the simulation results. In Fig. 5.3 the percentage of encircled energy on the target using nonlinear optimization of the image sharpness metric and using HWFS processing are compared. The curve marked NLOPT refers to the results obtained using nonlinear optimization of the image sharpness metric and the curve marked HWFS refers to the results obtained using a Hartmann wave front sensor and reconstructor. Figure 5.3 shows that for any given angle  $\theta_{mask}$  controlling the deformable mirror using nonlinear optimization-based techniques results in a much larger improvement in percentage of encircled energy than controlling the deformable mirror using parameters obtained from a Hartmann wave front sensor and reconstructor.

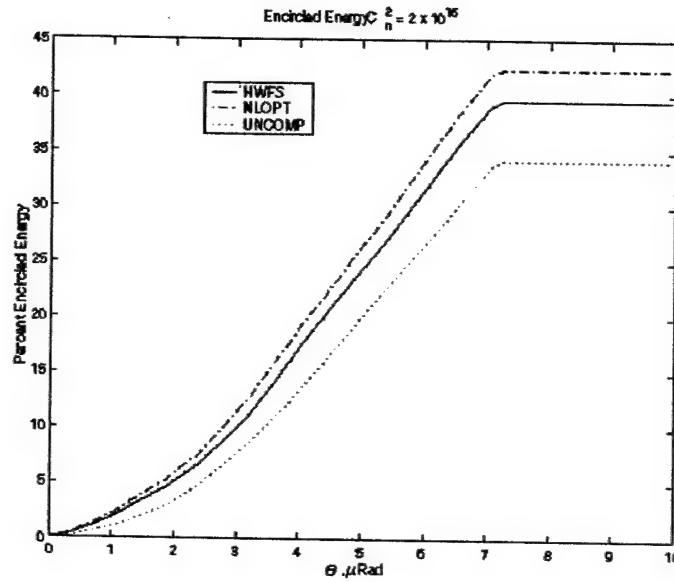


Figure 5.3. Percentage of ensemble average encircled energy in the target plane for  $C_n^2 = 2 \times 10^{-16} \text{ m}^{-2/3}$ , using  $\theta_{\text{mask}} = 0.0943 \text{ } \mu\text{Rad}$ , which leads to the highest percentage of encircled energy. HWFS result due to phase conjugation only without optimization.

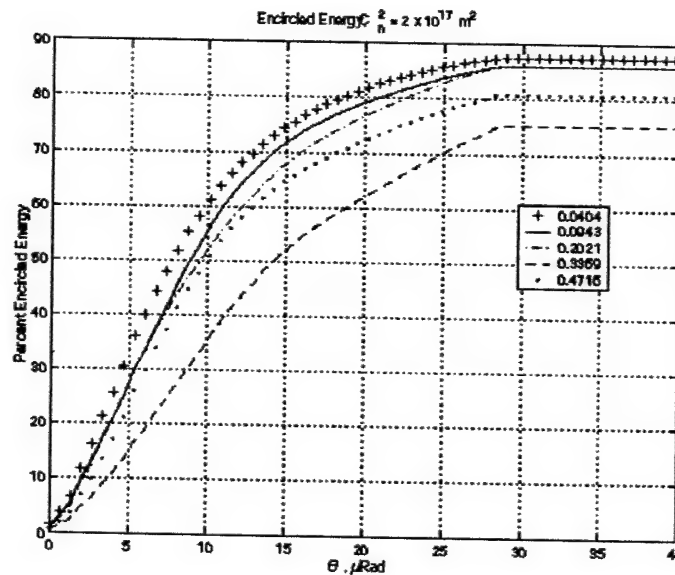


Figure 5.4. Percentage of ensemble average encircled energy in the target plane for  $C_n^2 = 2 \times 10^{-17} \text{ m}^{-2/3}$ . Using a  $\theta_{\text{mask}} = 0.0404 \text{ } \mu\text{Rad}$  leads to the highest percentage of encircled energy and smallest angle.

Figure 5.4 shows the encircled energy performance of this technique as the angular extent of the mask is gradually increased for the fixed turbulence strength of



$C_n^2 = 2 \times 10^{-17} \text{ m}^{-2/3}$ . We observe that, as expected, the performance is decreased as the mask diameter is increased at this relatively low turbulence strength. Figures 5.5 and 5.6 show similar plots for cases of increasing turbulence strength – in the case of Fig. 5.5  $C_n^2 = 5 \times 10^{-17} \text{ m}^{-2/3}$ , and in the case of Fig. 6  $C_n^2 = 2 \times 10^{-16} \text{ m}^{-2/3}$ . Interestingly, Figs. 5.5 and 5.6 show that the optimum mask width varies with turbulence strength and the general trend is that the mask diameter must be increased as the turbulence strength increases. The optimum mask diameter as a function of turbulence strength results are summarized in Table 5.1.

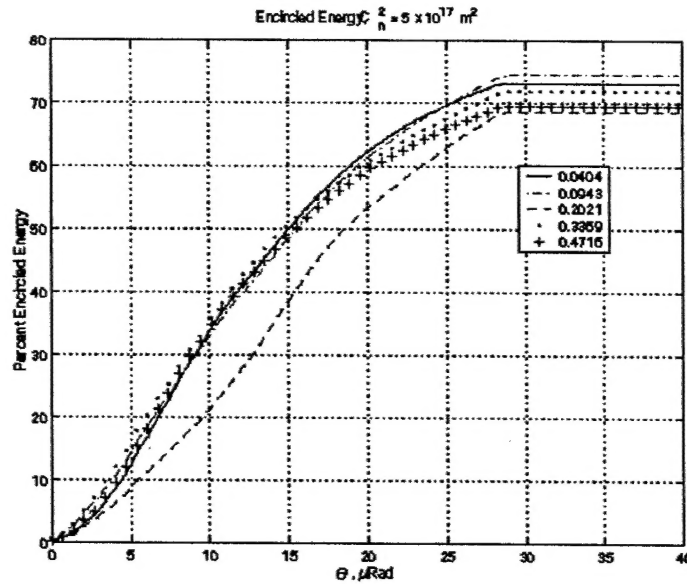


Figure 5.5. Percentage of ensemble average encircled energy in the target plane for  $C_n^2 = 5 \times 10^{-17} \text{ m}^{-2/3}$ . Using  $\theta_{\text{mask}} = 0.0943 \mu\text{Rad}$  leads to the highest percentage of encircled energy.

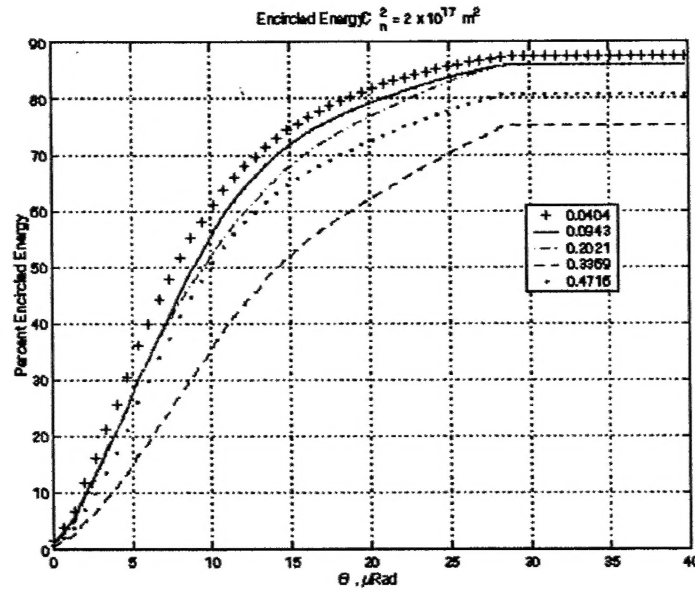


Figure 5.6. Percentage of ensemble average encircled energy in the target plane for  $C_n^2 = 2 \times 10^{-16} \text{ m}^{-2/3}$ . Using  $\theta_{mask} = 0.2021 \text{ } \mu\text{Rad}$  leads to the highest percentage of encircled energy.

Table 5.1. Optimum mask angular subtenses as a function of turbulence strength.

$C_n^2 (\times 10^{-17} \text{ m}^{-2/3})$	$\theta_{mask} (\mu\text{Rad})$	$\theta_0 (\mu\text{Rad})$	$\theta_{mask} / \theta_0$
2	4.04	2.04	1.98
5	33.39	1.18	28
20	9.43	0.51	18.49
70	9.43	0.24	39.29

In conclusion, a new approach to controlling a deformable mirror in beam projection systems operating in conditions of strong turbulence was introduced. It has been shown that the nonlinear optimization of an image sharpness metric can significantly improve the performance of the beam projection system. However, although the best radius of the mask's aperture was larger than expected, it subtends an angle that is only a few times larger than the isoplanatic angle.

**BIBLIOGRAPHY (Bold entries were published as a result of this contract.)**

1. T. Weyrauch, M.A. Vorontsov, T.G. Bifano, A. Tuantranont, V.M. Bright, J.R. Karpinsky, J.A. Hammer, "Performance evaluation of micromachined mirror arrays for adaptive optics", in *High-Resolution Wavefront Control: Methods, Devices, and Applications II*, J.D. Gonglewski, M.A. Vorontsov, and M.T. Gruneisen, Eds., *Proc. SPIE* 4124, pp. 32-41 (2000).
2. T. Weyrauch, M.A. Vorontsov, T.G. Bifano, M.K. Giles, "Adaptive optics system with micromachined mirror array and stochastic gradient descent controller," in *High-Resolution Wavefront Control: Methods, Devices, and Applications II*, J.D. Gonglewski, M.A. Vorontsov, and M.T. Gruneisen, Eds., *Proc. SPIE* 4124, pp. 178-188 (2000).
3. T. Weyrauch, M.A. Vorontsov, T.G. Bifano, J. Hammer, M. Cohen, and G. Cauwenberghs, "Micro-scale adaptive optics: wavefront control with a  $\mu$ -mirror array and a VLSI stochastic gradient descent controller," *Appl. Opt.* 40(24), 4243-4253 (2001).
4. T. Weyrauch and M.A. Vorontsov, "Dynamic wave-front distortion compensation with a 134-control-channel sub-millisecond adaptive system," *Opt. Lett.* 27(9), 751-753 (2002).
5. T. Weyrauch, M.A. Vorontsov, and J. W. Gowens, "Adaptive compensation of atmospheric effects with a high-resolution micro-machined deformable mirror," in *High-Resolution Wavefront Control: Methods, Devices, and Applications IV*, J.D. Gonglewski, M.A. Vorontsov, and M.T. Gruneisen, Eds., *Proc. SPIE* 4825, pp. 14-23 (2002).
6. Jungtae Rha, "Wave Front Sensing and Reconstruction Using a Twisted Nematic Liquid Crystal Device," Ph.D. Dissertation, New Mexico State University (May 2003).
7. M. K. Giles, C. Asbill, and B. Baker, "Design considerations for a miniature, portable, phase-contrast wave front sensor," *Proc. SPIE* 4825, pp. 207-214 (2002).
8. J. Rha and M. K. Giles, "Implementation of an adaptive Shack-Hartmann sensor using a phase-modulated liquid crystal spatial light modulator," *Proc. SPIE* 4493, pp. 80-87 (2001).
9. M. K. Giles, A. J. Seward, and T. M. Giles, "Closed-loop phase-contrast adaptive optics system using liquid crystal phase modulators: experimental results," *Proc. SPIE* 4493, pp. 174-183 (2001).

10. M. K. Giles, A. Seward, M. A. Vorontsov, J. Rha, and R. Jimenez, "Setting up a liquid crystal phase screen to simulate atmospheric turbulence," *SPIE Proceedings*, Volume 4124, pp. 89-97, August 1, 2000.
11. F. Zernike, "How I discovered phase contrast," *Science* **121**, 345-349 (1955).
12. A. Seward, F. Lacombe, and M. K. Giles, "Focal plane masks in adaptive optics systems," *Proc. SPIE* **3762**, 283-293 (1999).
13. M. A. Vorontsov, E. W. Justh, and L. A. Beresnev, "Adaptive optics with advanced phase-contrast techniques. I. High-resolution wave-front sensing," *J. Opt. Soc. Am. A* **18**, 1289-1299 (2001).
14. R. K. Tyson, *Principles of Adaptive Optics*, 2<sup>nd</sup> edition (Academic Press, 1998).
15. L. C. Roberts and C. R. Neyman, "Characterization of the AEOS Adaptive Optics System," *Pub. Astron. Soc. Pac.* **114**, 1260-1266, 2002.
16. R. D. Fiete and T. Tantaló, "Comparison of SNR image quality metrics for remote sensing systems," *Opt. Eng.* **40**, 574-585, 2001.
17. N. Clark, "Spatial light modulator having amplitude coupled with binary phase mode," U.S. Patent Number 5,535,029, July 9, 1996.
18. D. M. Cottrell, J. A. Davis, T. R. Hedmann, and R. A. Lilly, "Multiple imaging phase-encoded optical elements written on programmable spatial light modulators," *Appl. Opt.* **29**, 2505-2509 (1990).
19. Vincent Laude, "Twisted-nematic liquid-crystal pixilated active lens," *Optics Communications* **153**, 134-152 (1998).
20. Rensheng Dou, "Wavefront control using a liquid crystal television," Ph.D Dissertation, New Mexico State University, Chapter 4, (May 1996).
21. Narasimha S. Prasad, Sean M. Doyle, and Michael K. Giles, "Collimation and beam alignment: testing and estimation using liquid-crystal televisions," *Opt. Engrg*, **35**, 1815-1819 (July 1996).